

AFML-TR-71-74

**BASELINE SOLUTIONS FOR THE SMOOTH WALL  
THERMOCHEMICAL ABLATION RESPONSE  
OF GRAPHITE AND CARBON PHENOLIC**

*R. A. RINDAL*

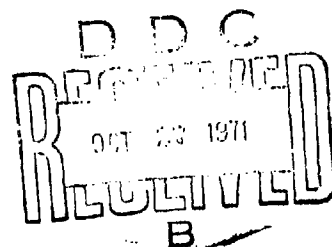
*M. R. WOOL*

*C. A. POWARS*

*AEROTHERM CORPORATION*

TECHNICAL REPORT AFML-TR-71-74

JULY 1971

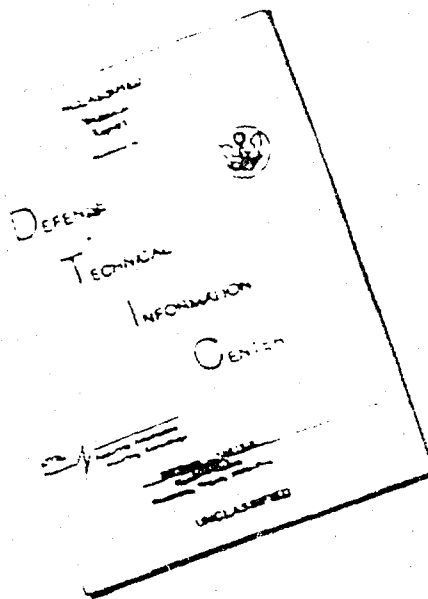


Approved for public release; distribution unlimited

Reproduced by  
**NATIONAL TECHNICAL  
INFORMATION SERVICE**  
Springfield, Va. 22151

**AIR FORCE MATERIALS LABORATORY  
AIR FORCE SYSTEMS COMMAND  
WRIGHT-PATTERSON AIR FORCE BASE, OHIO**

# DISCLAIMER NOTICE



THIS DOCUMENT IS BEST  
QUALITY AVAILABLE. THE COPY  
FURNISHED TO DTIC CONTAINED  
A SIGNIFICANT NUMBER OF  
PAGES WHICH DO NOT  
REPRODUCE LEGIBLY.

REPRODUCED FROM  
BEST AVAILABLE COPY

UNCLASSIFIED

Security Classification

DOCUMENT CONTROL DATA - R & D		
<i>(Security classification of title, body of abstract and indexing annotation must be entered when the overall report is classified)</i>		
1. ORIGINATING ACTIVITY (Corporate author) Aerotherm Corporation 485 Clyde Avenue Mountain View, California 94040		2a. REPORT SECURITY CLASSIFICATION UNCLASSIFIED 2b. GROUP
3. REPORT TITLE Baseline Solutions for the Smooth Wall Thermochemical Ablation Response of Graphite and Carbon Phenolic		
4. DESCRIPTIVE NOTES (Type of report and inclusive dates) Final Report, 1 March 1970 through 30 October 1970		
5. AUTHOR(S) (First name, middle initial, last name) R. A. Rindal, M. R. Wool, C. A. Powars		
6. REPORT DATE July 1971	7a. TOTAL NO. OF PAGES 59	7b. NO. OF REFS 28
8a. CONTRACT OR GRANT NO. F33615-69-C-1626, P003 b. PROJECT NO. 7381 c. Task 738102 d.	9a. ORIGINATOR'S REPORT NUMBER(S) Aerotherm Final Report No. 70-21 9b. OTHER REPORT NO(S) (Any other numbers that may be assigned this report) AF-71-74	
10. DISTRIBUTION STATEMENT Approved for Public Release; Distribution Unlimited		
11. SUPPLEMENTARY NOTES None		12. SPONSORING MILITARY ACTIVITY Air Force Materials Laboratory (LAS) Wright Patterson Air Force Base Ohio 45433
13. ABSTRACT Recently acquired high pressure ablation data for graphite and carbon phenolic are analyzed with the objective of establishing the magnitude of discrepancies between measured ablation rates and smooth-wall "thermochemical only" predictions. Data were obtained under the SAMSO sponsored Thermal Protection Program and are believed of sufficient quality to reach meaningful conclusions with respect to the magnitude of ablation enhancement resulting from the combined effects of rough-wall and mechanical erosion phenomena. Comparisons between predicted and measured recession are presented for laminar and turbulent conditions for models tested in the Cornell Wave Superheater, the AFFDL 50 MW arc-jet, and the AEDC ballistic range. The ratio of predicted-to-measured recession for laminar and turbulent flow for both materials correlate moderately well with local pressure.		

DD FORM 1473  
1 NOV 65

UNCLASSIFIED

Security Classification

# NOTICE

When Government drawings, specifications, or other data are used for any purpose other than in connection with a definitely related Government procurement operation, the United States Government thereby incurs no responsibility nor any obligation whatsoever; and the fact that the government may have formulated, furnished, or in any way supplied the said drawings, specifications, or other data, is not to be regarded by implication or otherwise as in any manner licensing the holder or any other person or corporation, or conveying any rights or permission to manufacture, use, or sell any patented invention that may in any way be related thereto.

ACCESSION for	
CFSTI	WHITE SECTION <input checked="" type="checkbox"/>
DDC	BLUE SECTION <input type="checkbox"/>
UNANNOUNCED	<input type="checkbox"/>
JUSTIFICATION	
BY	
DISTRIBUTION/AVAILABILITY CODES	
DIST.	ANAL. USE OF SPECIAL
A	

Copies of this report should not be returned unless return is required by security considerations, contractual obligations, or notice on a specific document.

UNCLASSIFIED  
Security Classification

14	KEY WORDS	LINK A		LINK B		LINK C	
		ROLE	WT	ROLE	WT	ROLE	WT
	ABLATION GRAPHITES CARBON/PHENOLIC COMPOSITES THERMOCHEMISTRY						

UNCLASSIFIED  
Security Classification

**BASELINE SOLUTIONS FOR THE SMOOTH WALL  
THERMOCHEMICAL ABLATION RESPONSE  
OF GRAPHITE AND CARBON PHENOLIC**

*R. A. RINDAL*

*M. R. WOOL*

*C. A. POWARS*

Approved for public release; distribution unlimited


#### ABSTRACT

Recently acquired high pressure ablation data for graphite and carbon phenolic are analyzed with the objective of establishing the magnitude of discrepancies between measured ablation rates and smooth-wall "thermochemical only" predictions. Data were obtained under the SAMSO sponsored Thermal Protection Program and are believed of sufficient quality to reach meaningful conclusions with respect to the magnitude of ablation enhancement resulting from the combined effects of rough-wall and mechanical erosion phenomena. Comparisons between predicted and measured recession are presented for laminar and turbulent conditions for models tested in the Cornell Wave Superheater, The AFFDL 50 MW arc-jet, and the AEDC ballistic range. The ratio of predicted-to-measured recession for laminar and turbulent flow for both materials correlate moderately well with local pressure.

## FOREWORD

The research work reported herein was conducted by Aerothelm Corporation, Mountain View, California for the Air Force Materials Laboratory, Air Force Systems Command, Wright Patterson Air Force Base, Ohio, under amendment number P003, USAF Contract F33615-69-C-1626. The effort was initiated under Project 7381, Task 738102, "Space, Missile and Propulsion Systems Material and Component Evaluation". The work was administered under the direction of Dr. Merrill L. Minges, Space and Missiles Systems Support Branch. The report covers work performed during the period March 1970 to October 1970.

This technical report has been reviewed and is approved.



L. N. Hjelm, Chief  
Space and Missiles Systems  
Support Branch  
Materials Support Division  
AF Materials Laboratory



# TABLE OF CONTENTS

<u>SECTION</u>		<u>PAGE No.</u>
1	INTRODUCTION	1
2	ABLATION AND STRUCTURAL ANALYSIS COMPUTER CODES	3
3	MATERIAL RESPONSE PREDICTIONS	6
	3.1 Ballistic Range Experiments	6
	3.1.1 Test Conditions	6
	3.1.2 Inviscid Flow Solutions	8
	3.1.3 Boundary Layer Solutions	11
	3.1.4 Comparison of Measured and Predicted Ablation Responses	20
	3.1.5 Thermal Expansion Calculations	20
	3.2 Wave Superheater and 50 MW RENT Facility Tests	29
	3.2.1 Test Conditions and Model Contours	32
	3.2.2 Inviscid Flow Representation	40
	3.2.3 Boundary Layer Solutions	42
	3.2.4 Ablation Response	46
	3.2.4.1 Effect of Uncertainties	46
	3.2.4.2 Comparison of Predictions with Data	47
4	CONCLUSIONS	55
	REFERENCES	58

# LIST OF FIGURES

<u>FIGURE</u>		<u>PAGE NO.</u>
1	Typical Overall Ballistic Range Model Geometry Shots 1750, 1756 (POCO Graphite)	9
2	Ballistic Range Model Velocity Histories	9
3	Stagnation Pressure Histories	10
4	Stagnation Enthalpy Histories	10
5	Hypersonic Pressure Ratio Distribution over Sphere-Cones	12
6	Hypersonic Shock Shape for Sphere-Cones	12
7	Comparisons of Transfer Coefficient Distributions	13
8	Effect of Edge Entropy Model on Boundary Layer Velocity Profiles	13
9	Effect of Boundary Layer Development on Velocity Profiles	15
10	Predicted Transfer Coefficient Distributions	16
11	Typical Boundary Layer Composition Profiles	18
12	Equilibrium Surface Thermochemical Ablation Data	21
13	Material Thermal Conductivity Data	22
14	Predicted Surface Temperature Histories	23
15	In-Depth Thermal Responses	25
16	Comparison of Predicted and Measured Model Recession	27
17	Finite Element Analysis of Ballistic Range POCO Model (Test No. 1750)	30
18	Stream Centerline Impact Pressure Decay with Axial Distance	33
19	Ablated Nose Contour from Film Data and Nose Geometry Employed in the Analysis	35

# LIST OF FIGURES (conc.)

<u>FIGURE</u>		<u>PAGE NO.</u>
20	Ablation Model Response Data	37
21	Model Pressure Distributions	43
22	Effect of Uncertainties Upon Predicted Ablation Rate	49
23	Comparison of Measured and Predicted Axial Recession Rate	52
24	Correlation of Predicted to Measured Recession Rate with Local Pressure	56

## SECTION 1

### INTRODUCTION

The objective of this study was to calculate the smooth wall, thermochemical, steady-state ablation response of selected reentry vehicle nose tip models tested as part of the SAMSO, Aerospace Thermal Protection Program. Calculations were performed for POCO graphite and R-6300 carbon-phenolic models tested in the Cornell Wave Superheater, the AFFDL 50 MW RENT facility, and the AEDC Hypervelocity Range G facility. These calculations specifically exclude the effects of the rough model surface on heat and mass transfer rates and the effects of mechanical ablation on the model response. Thus, these predictions provide an accurate "baseline" for comparison to experimentally observed ablation response, and these comparisons provide useful input to mechanical ablation and surface roughness effects studies.

The test conditions and model contours for the ablation response predictions were taken from References 1 and 2 for models tested in the CAL WSH, from Reference 3 for models tested in the RENT facility, and from References 4 and 5 for models tested in the ballistic range. The selection of the particular models for analysis was guided by the desire to consider (1) a variety of materials, (2) a variety of test facilities and conditions, and (3) relatively high quality test data, particularly contour histories. "Baseline" smooth-wall thermochemical ablation response predictions were performed for the following models:

<u>Model No.</u>	<u>Test Facility</u>	<u>Material</u>
G-9	WSH	POCO graphite
CP-16	WSH	R-6300 carbon phenolic
12-2	RENT	POCO graphite
103A	RENT	R-6300 carbon phenolic
123A	RENT	R-6300 carbon phenolic
1750	Ballistic Range	POCO graphite
1756	Ballistic Range	POCO graphite
1763	Ballistic Range	R-6300 carbon phenolic
1861	Ballistic Range	R-6300 carbon phenolic

In addition to performing "baseline" thermochemical ablation calculations, a number of parametric calculations for one of the models tested in the wave superheater were performed in order to quantitatively assess the effects of several uncertainties and assumptions on the computed ablation responses. The uncertainties assessed in this fashion were:

- o Uncertainties associated with defining the model contour from the reduced movie film data - nose radius and bi-conic cone angle uncertainties
- o Transition location uncertainties
- o The effect of the pressure distribution representation
- o The effect of unequal species diffusion coefficients for carbon phenolic ablation
- o The effect of the "enthalpy spike" in the AFFDL 50 MW RENT facility.

The analytical techniques employed in these computations are briefly described in Section 2. The baseline model response predictions are compared to measurements in Section 3, and appropriate conclusions are drawn in Section 4.

## SECTION 2

### ABLATION AND STRUCTURAL ANALYSIS COMPUTER CODES

In this section, the computerized analytical tools utilized in this program are described. These codes evaluate the fluid dynamics, boundary layer mass and heat transfer, surface thermochemistry, transient in-depth heat conduction, and thermal-structural response phenomena. The various codes are described in the following paragraphs.

#### AEROTHERM CHEMICAL EQUILIBRIUM (ACE) CODE

The ACE code evaluates the equilibrium or kinetically controlled chemical composition of a set of molecular species and associated thermodynamic and transport properties for two types of systems; closed systems and open systems. In a closed system calculation, the relative amounts of each element in the total system plus system pressure and either system entropy, temperature, or enthalpy are specified. For an open system calculation, the relative amounts of the chemical elements depend upon various boundary layer mass transfer formulations and upon the specified injection rates of solid material decomposition products and surface ablation products. Chemical equilibrium with a solid surface species provides an additional constraint in open system computations. Further descriptions of ACE code options are included in References 6, 7 and 8.

#### INVISCID FLOW CODES, RABBI AND SUPER

Surface pressure distributions and bow shock shapes are obtained utilizing two computer codes, one for the solution of the subsonic and transonic nose region, (Realgas Axisymmetric Blunt Body at Incidence, Refs. 9 and 10), and the other for the solution of the supersonic regions. (SUPER, Ref.11) Solutions in the subsonic/transonic region performed in this study were obtained using a zero angle of attack version of RABBI code described in Reference 10. The steady flow field was obtained as the time asymptotic limit of an unsteady flow. The shock was treated as a sharp discontinuity. The code is applicable to thermally and calorically perfect gases or to air in chemical equilibrium (perfect gas equation of state).

The supersonic flow field program (SUPER) employs the method of characteristics as described in Reference 11. All shocks are treated as sharp discontinuities; sharp expansion corners are treated as concentrated centered

expansions; the fluid is treated as a thermally and calorically perfect gas. The initial data for this code is obtained from the RABBI code, described in the preceding paragraph.

In order to make a consistent coupling between the two codes, the solution in the subsonic/transonic region is done for an ideal gas (here,  $\gamma=1.2$  was used.). The solutions were compared with the solutions for air in equilibrium, and it was found that there was no difference in surface pressure distribution and negligible difference in the bow shock shape.

#### BOUNDARY LAYER INTEGRAL MATRIX PROCEDURE (BLIMP)

The BLIMP code computes numerical solutions of the nonsimilar multi-component laminar and/or turbulent boundary layer with arbitrary equilibrium or nonequilibrium chemically reacting systems over planar or axisymmetric bodies. A variety of surface boundary conditions, including coupling with steady state or transient charring ablation energy and mass balances, are available. Multi-component diffusion and thermal diffusion are treated through the use of convenient correlation equations. The code computes its own boundary layer edge condition from the stagnation conditions, the pressure distribution, and, if entropy layer is being considered, shock shape input data.

The numerical solution method, termed an integral-matrix procedure and described in References 12, 13 and 14, incorporates sets of connected quadratics between boundary layer nodal points to relate enthalpy, velocity, and elemental mass fraction variations to their derivatives with respect to the boundary layer thickness coordinate. The derivatives of these quadratics are made continuous at the nodal points thus resulting in smooth but flexible profiles. The turbulent flow model built into the BLIMP code consists of dividing the flow into a wall region in which a mixing length description of turbulent shear is used and a wake region in which eddy viscosity is related to global parameters of the flow. Further discussion of the BLIMP code including descriptions of the turbulent model are included in Reference 15, 16 and 17.

#### CHARRING MATERIAL ABLATION (CMA) PROGRAM

The CMA program computes the in-depth transient thermal response of a one-space dimension charring, ablating material. An Arrhenius rate law is utilized to obtain material decomposition in-depth. The program is an implicit, finite-difference computational procedure for heat conduction coupled to one of three ablating surface boundary conditions. These options are:

- A film coefficient model which accounts for convection - radiation heating with coupled mass transfer, including the effects of unequal heat and mass transfer, unequal species diffusion rates, and surface chemical reactions in equilibrium or kinetically controlled.
- Specified surface temperature and recession rate.
- Specified radiation view factor and incident radiation flux for a stationary surface.

For the first and last options a surface energy balance is utilized in conjunction with the in-depth implicit finite difference solution to define surface temperature. Surface temperature is specified in the second option. Surface thermochemistry data generated by the ACE code is utilized by the first option. Additional descriptions of the use and operation of the CMA code are included in References 18, 19 and 20.

#### AXISYMMETRIC TRANSIENT HEATING AND MATERIAL ABLATION (ASTHMA) PROGRAM

The ASTHMA code is a two space dimension transient heat conduction code for ablating but non-charring materials. It accounts for two-dimensional surface recession, and allows for anisotropic in-depth thermal conduction. Surface boundary conditions are in general the same as those described above for the CMA code. Input to the ASTHMA code consists of geometry specifications (in terms of a finite difference grid), material thermal properties tables, and heated surface boundary condition information as a function of time. Output consists of two dimensional thermal properties and surface recession. Provision is made for subsequent input of thermal data into various structural analyses codes. Further description of the code are included in Reference 21 and addenda thereto.

#### DEFORMATION FORMULATION OF ORTHOTROPIC AXISYMMETRIC SOLUTION OF INELASTIC SOLIDS (DOASIS)

The DOASIS finite element stress analysis code determines the anisotropic, elastic-plastic-thermal solution (i.e. displacements, stresses, strains, etc.) of any two dimensional structure (axisymmetric, plane stress or plane strain) for any prescribed mechanical and/or thermal load. The inelastic response is based on deformation plasticity theory, in conjunction with the appropriate orthotropic material formulation. The finite element method of solution is employed which subdivides the structure into a number of "finite elements" with nodes. The solution consists of finding the displacements of these nodes and then the resulting strains and stresses in each finite element. When inelastic phenomenon occurs, the nonlinear solution is found by iteration. Further details of the theory and methodology of the DOASIS code may be found in References 22 and 23.



## SECTION 3

### MATERIAL RESPONSE PREDICTIONS

This section presents experimental data, describes how the baseline calculations were performed, and compares predicted to measured model response. Calculations for the ballistic range experiments are presented in Section 3.1 and are followed, in Section 3.2 by a description of calculations for the wave superheater and the 50 MW RENT facility.

#### 3.1 BALLISTIC RANGE EXPERIMENTS

The recent improvements in the instrumentation and data acquisition capabilities of the AEDC 1000 ft Ballistic Range facility have enabled experimental data to be obtained for conditions closely approximating those encountered by high performance reentry vehicles. These data should be useful not only in experimentally verifying the applicability and survivability of new heat shield materials, but also in the evaluation and improvement of analytical techniques for the prediction of material response. In this section, detailed predictions of the thermal response of four model shots in the AEDC Range G facility during the recently completed SAMSO/Aerospace test program] are described. Comparisons between predictions and test measurements provide a basis for assessing the quality of the data and the current analytical techniques. The predictions were performed utilizing the computer codes described above in Section 2. The test conditions of the range shots for which the calculations correspond are given in Section 3.1.1. The inviscid flow solution (shock shape and pressure distribution) are presented in Section 3.1.2. Results of boundary layer computations are discussed in Section 3.1.3. The surface and in-depth transient thermal response predictions (including recession) are shown in Section 3.1.4. And the evaluation of model thermal expansion during one of the range shots is described in Section 3.1.5.

##### 3.1.1 Test Conditions

Four ballistic range shots were selected for analysis in this study. The test conditions, model geometries and materials are summarized in Table I. All four shots were performed in the AEDC 1000 ft ballistic range[during the SAMSO/Aerospace test program.] Two shots for each of two materials were chosen for these calculations to demonstrate the effect of both different materials

TABLE 1

SUMMARY OF BALLISTIC RANGE SHOTS				
SHOT No.	1750	1756	1763	1861
Material (Layup Angle)	POCO	POCO	R-6300 (30°)	R-6300 (30°)
Range Temperature (°F)	75°	75°	75°	75°
Range Static Pressure (atm)	0.364	0.458	0.366	0.236
Blast Tank Static Pressure (atm)	0.013	0.038	0.037	0.026
Launch Velocity (ft/sec)	17860	17000	17900	18580
Time to Last Station <sup>a</sup> (millisec)	57.9	62.1	56.9	52.2
Initial Geometry (Sphere-Biconic)				
Nose Radius (inches)	0.040	0.040	0.040	0.045
Fore Cone Half Angle (Deg.)	45°	45°	40°	37.5°
Aft Cone Half Angle (Deg.)	16°	16°	16°	16°
Ballistic Coefficient (psf)	58	58	58	78
Init. Stag. Pt. Pressure <sup>b</sup> (atm)	122.1	139.2	123.3	85.8
Init. Stag. Pt. Enthalpy <sup>c</sup> (Btu/lbm)	6372	5773	6400	6896
Stag. Pt. Recession <sup>d</sup> (mils)	25	24	44	36

(a) Time from launch, Station 42 (940 ft., including blast tank)

(b) Entrance to range tank.

(c) JANAF base state, 298°K.

(d) Station 42.

and varying test conditions. In-flight model profile traces and the corresponding recession measurements were studied to define those shots which provided the most consistent set of response data. Shots were graded not only on the clarity and resolution of the stagnation point recession measurements, but also on the degree of symmetry and quality of shape data on the fore-cone section of the model. Hence data for the shots predicted should provide valuable comparisons for both the laminar nose region and the turbulent cone region. The two materials for which predictions were performed (POCO graphite and R-6300 carbon phenolic) are representative of currently utilized reentry vehicle thermal protection systems. Figure 1 shows the overall shape of the two POCO graphite models.

Model velocity histories determined from test data for each shot are shown in Figure 2. The velocity decay is due to aerodynamic drag on the test model. Based upon real gas computations of flow past a normal shock wave (ACE code), the stagnation point enthalpy and pressure histories were obtained from the range static conditions and the velocity histories. Stagnation point pressure and enthalpy histories are shown in Figures 3 and 4, respectively, for each range shot considered. These histories along with the inviscid flow solution discussed in the following section provide the necessary input to the boundary layer and thermal structural calculations.

### 3.1.2 Inviscid Flow Solutions

The inviscid flow about the ballistic range model is one of the primary inputs to the evaluation of the boundary layer flow and the model thermal-structural response. An inviscid flow solution for a particular body geometry consists of the bow shock wave geometry and the associated pressure gradients. To evaluate these, the RABBI and SUPER codes discussed in Section 2 were utilized assuming ideal gas flow ( $\gamma = 1.2$ ). For the hypersonic conditions of interest here (Mach numbers between 11.0 and 16.5), effects of varying stagnation pressure and Mach number on shock shape and pressure distribution are negligible. This was verified by performing calculations at various free stream conditions for the  $45^\circ$  half-angle sphere-cone nose geometries used in shots 1750 and 1756 and shown in Figure 1.

The variation of model geometry due to ablation during flight does alter the inviscid flow. To account for this variation, in-flight model profile traces were utilized to define approximate shapes for each time at which boundary layer solutions were obtained. Because of the extremely short exposure times ( $\approx 60$  milliseconds), recession was small so that, although ablation occurred, the models remained roughly sphere-cones. That is, ablation resulted in only slight increases in the nose radii and for the R-6300 models slight decreases in the cone half angle. As a result, sphere-cone solutions of the

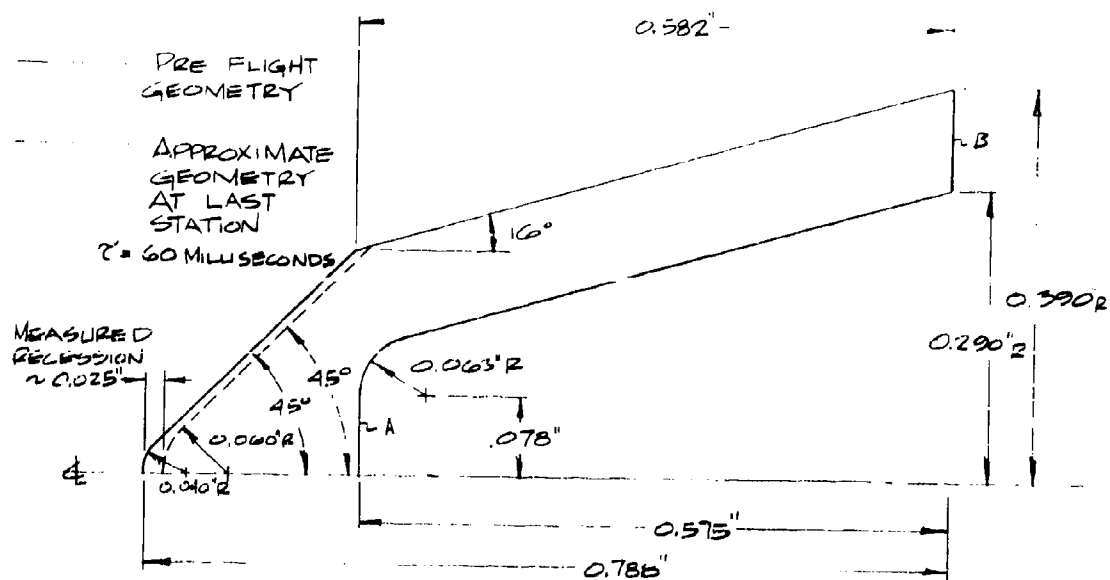


FIGURE 1 TYPICAL OVERALL BALLISTIC RANGE MODEL GEOMETRY  
SHOTS 1750, 1756 (POCO GRAPHITE)

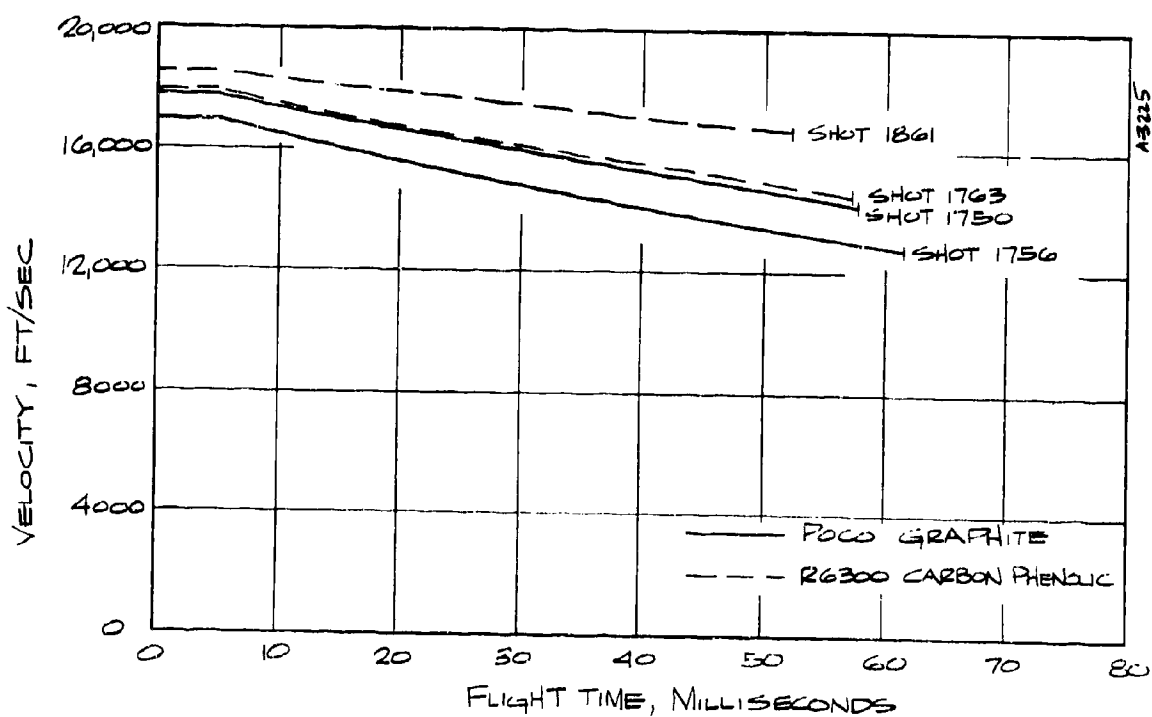


FIGURE 2 BALLISTIC RANGE MODEL VELOCITY HISTORIES

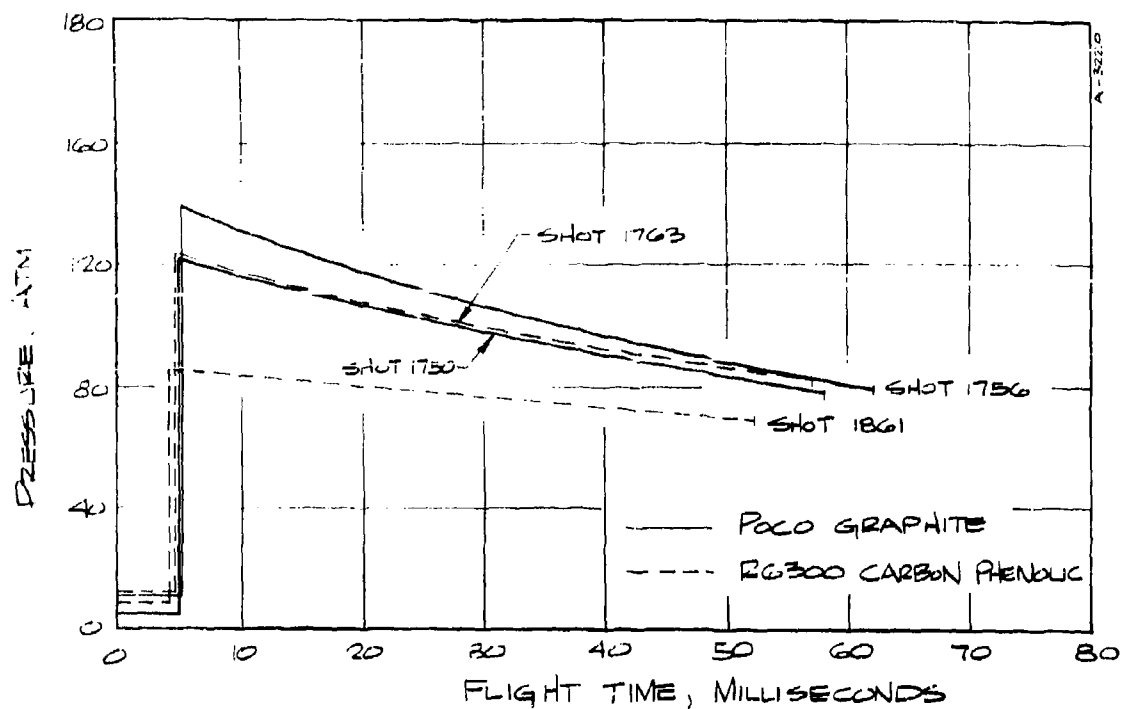


FIGURE 3 STAGNATION PRESSURE HISTORIES

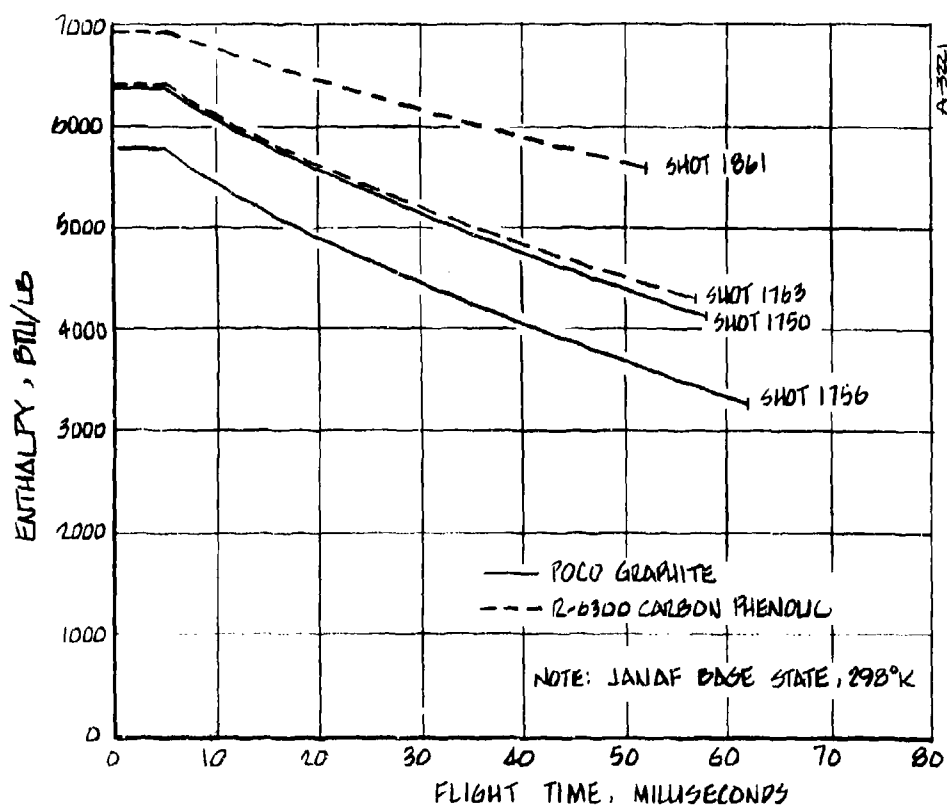


FIGURE 4 STAGNATION ENTHALPY HISTORIES

inviscid flow could be used throughout. This provided a great simplification since inviscid flow solutions are identical for any similar geometrical shape. Figure 5 shows the variation of pressure ratio with normalized stream dimension and Figure 6 gives the shock angle as a function of normalized radius (from the body centerline) to the shock. The solution for the  $45^\circ$  half angle cone was used for all POCO graphite model solutions while the solutions between  $35^\circ$  and  $40^\circ$  were utilized for the various geometries obtained by the R-6300 models.

### 3.1.3 Boundary Layer Solutions

The BLIMP code described in Section 2 was utilized to compute the heat transfer coefficient distributions around the ballistic-range models for several times during each shot analyzed. The solutions accounted for the variations in free stream conditions, model geometry, and shock shape as described above. Cross plots of transfer coefficient versus time for the body locations of interest provided the coefficient histories required as input to the thermal response codes.

The BLIMP solutions for both the POCO and the R-6300 models were performed utilizing a surface energy balance formulation which accounts for steady state ablation of the nose tip material in thermochemical equilibrium with the gas at the surface. Also, the assumption of equal diffusion coefficients for all species in the boundary layer was utilized. This assumption is further discussed in Section 3.2 below. No attempt was made to account for surface roughness in these boundary layer calculations.

The effect of the large entropy gradient at the boundary layer edge due to the shock wave curvature was quite significant in these solutions. This entropy gradient occurs because the mass at different locations in the boundary layer and the edge gas has entered the flow through different shock angles. In regions where the shock curvature changes rapidly, this entropy layer results in an edge vorticity much different than zero. The effect on the predicted heat transfer coefficient distribution is shown in Figure 7. Several other solutions for the same geometry are shown for comparison. As would be expected, the entropy layer solution near the stagnation point is near the solution found using only a normal shock entropy, while out on the conic region, the entropy layer solution approaches that obtained using sharp cone shock angle to define the edge entropy. Velocity profiles at a streamwise location of 0.008 feet for the three distributions are shown in Figure 8. In the figure, edge velocity is used to normalize the local velocity in the boundary layer. The effect of the vorticity (i.e., the entropy layer) is to produce the non-zero slope in profile at the boundary layer edge.

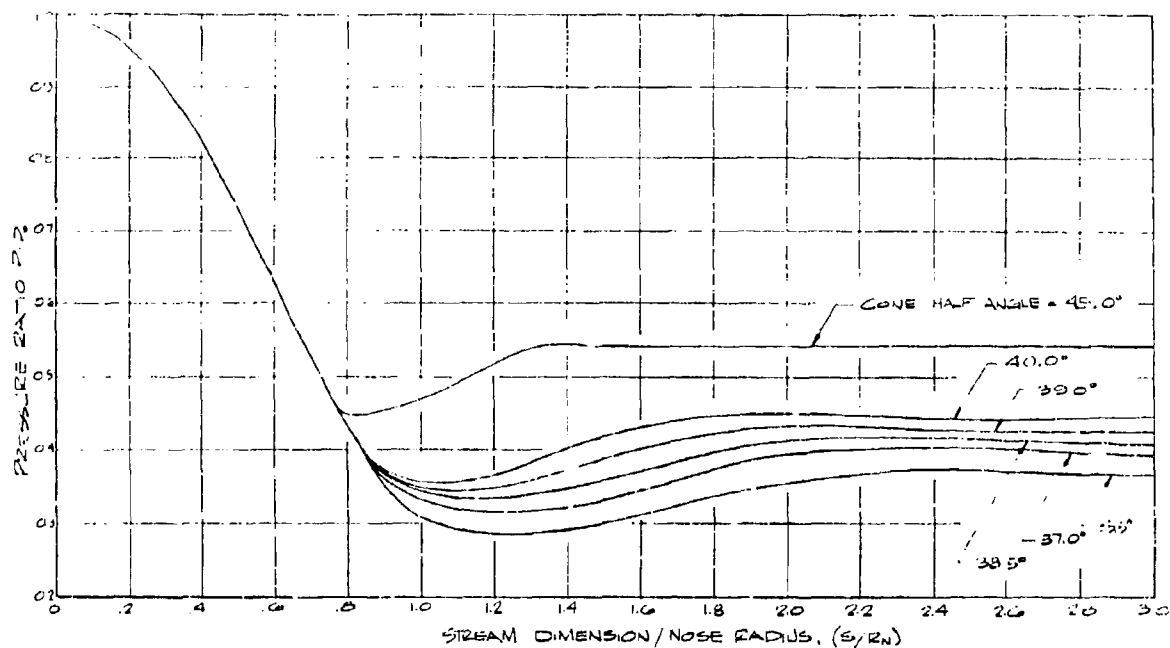


FIGURE 5 HYPersonic PRESSURE RATIO DISTRIBUTION OVER SPHERE-CONES,  
 $\gamma = 1.2$ , MACH  $N^{\circ} > 10$ .

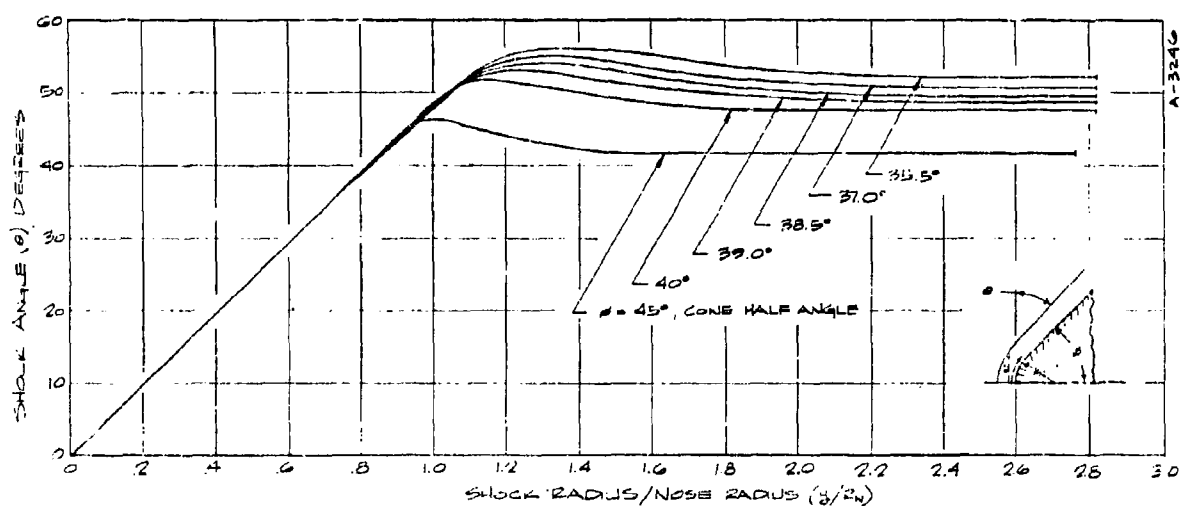


FIGURE 6 HYPersonic SHOCK SHAPE FOR SPHERE-CONES,  
 $\gamma = 1.2$ , MACH  $N^{\circ} > 10$

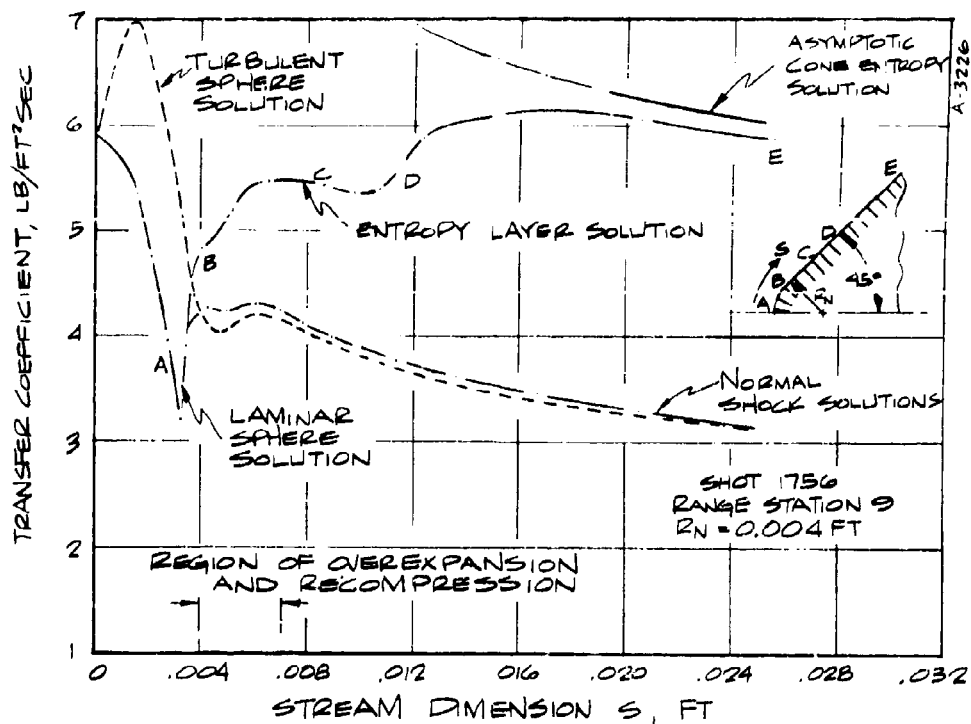


FIGURE 7 COMPARISONS OF TRANSFER COEFFICIENT DISTRIBUTIONS

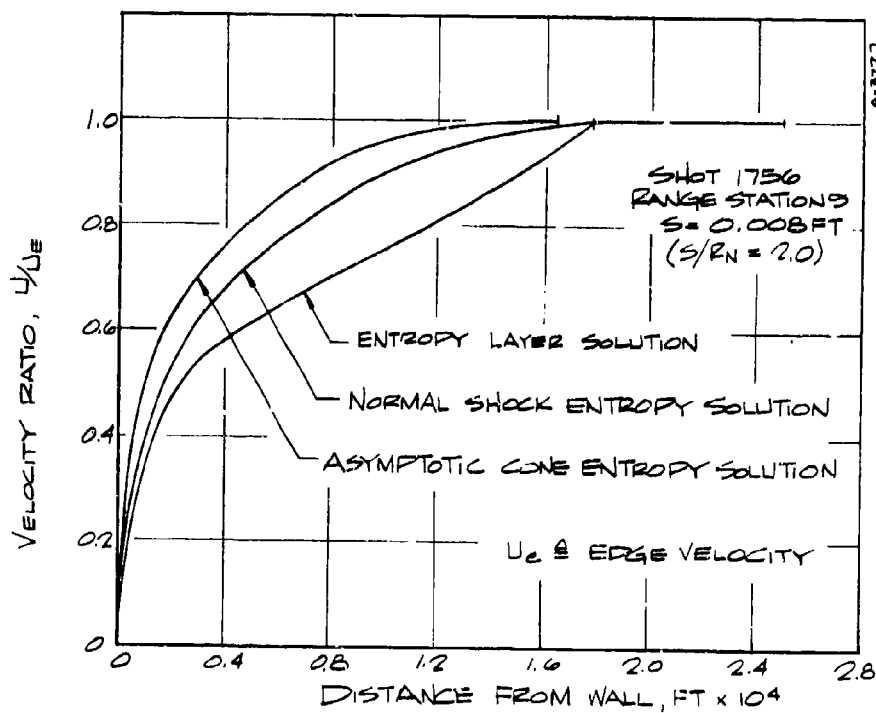


FIGURE 8 EFFECT OF EDGE ENTROPY MODEL ON BOUNDARY LAYER VELOCITY PROFILES



The minimum point in the coefficient distribution (at a streamwise location of 0.010 feet) of Figure 7 occurs because the edge vorticity passes through a maximum at this point. The velocity gradients within the boundary layer are least severe and the minimum in coefficient results. Some question exists as to the reality of this edge vorticity effect on the coefficient distributions. During the running of the various BLIMP solutions considerable difficulty was encountered in several cases at this location on the body. Convergence was often defeated by apparent instabilities in the numerical technique or in the turbulent model being employed. At times, more than one solution appeared mathematically possible. Once past this region, the solutions were quickly obtained and appeared correct. As seen in Figure 7, downstream of the minimum the solution approaches that for the sharp cone since edge vorticity decreases to zero and edge entropy approaches the sharp cone shock angle value.

A feeling for the development of the boundary layer can be obtained from Figure 9. Shown are five velocity profiles for various locations on the body. Local velocity in this figure is normalized by a reference velocity (the velocity which is calculated for an isentropic expansion to the local pressure ratio for a normal shock). Notice that due to entropy layer this reference velocity can be less than the computed edge velocity. The five profiles shown correspond to the following body locations:

- A - Laminar profile near sonic point
- B - First turbulent profile
- C - Solution upstream of vorticity maximum showing entropy layer effects
- D - Solution downstream of vorticity maximum showing boundary layer thinning due to entropy layer effects
- E - Last solution approaching sharp cone profile.

The heat transfer coefficient distributions for each BLIMP solution performed in this study are shown in Figure 10. The trends discussed above occur throughout although the locations and degree of severity change because of the varying test conditions and geometries. For the two carbon phenolic shapes, predictions were carried out only to the middle of the fore cone where the last CMA calculation was performed. Examples of typical boundary layer composition profiles are shown in Figure 11. One is for a POCO graphite prediction and one is for an R-6300 carbon phenolic prediction.

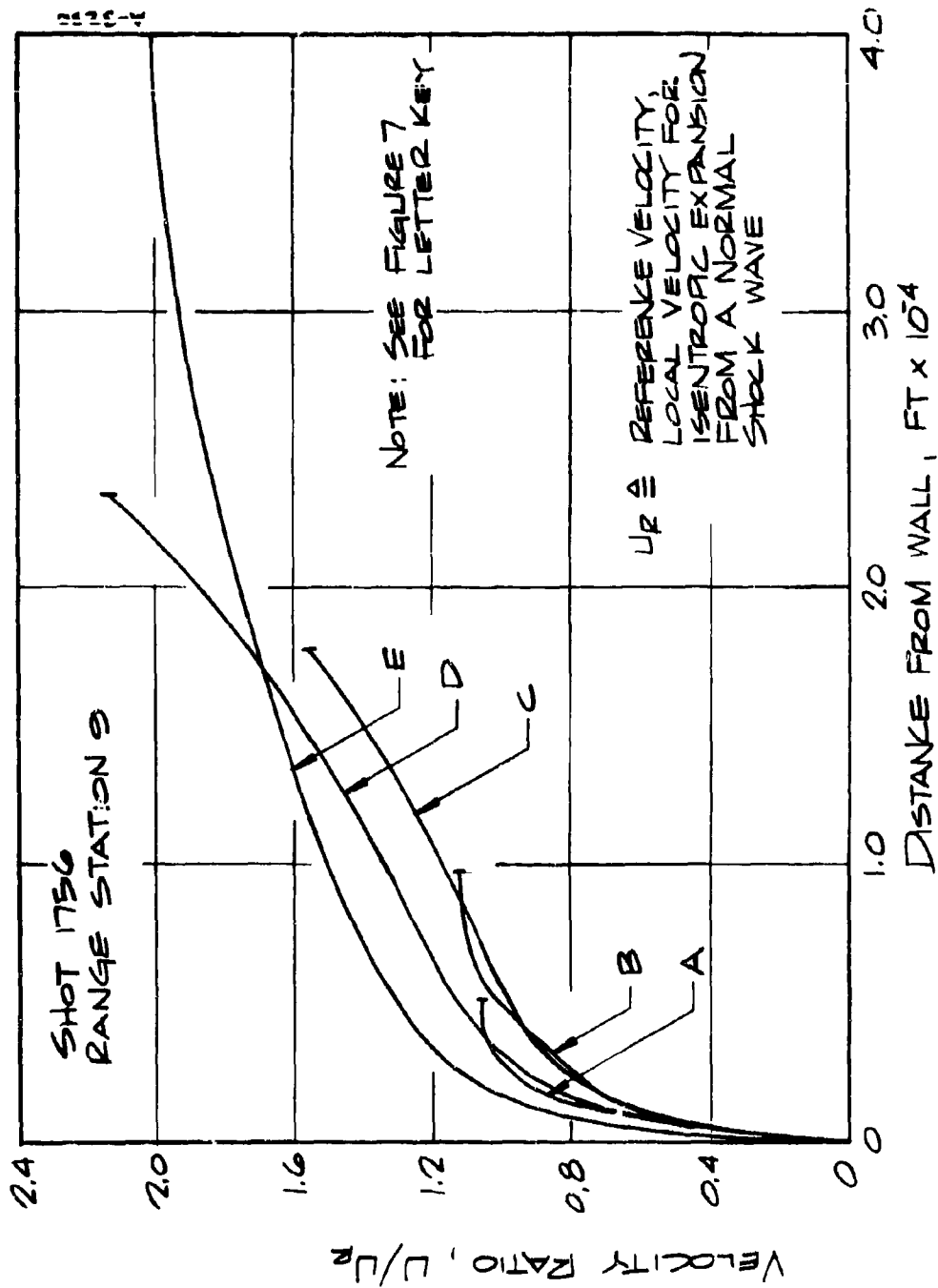
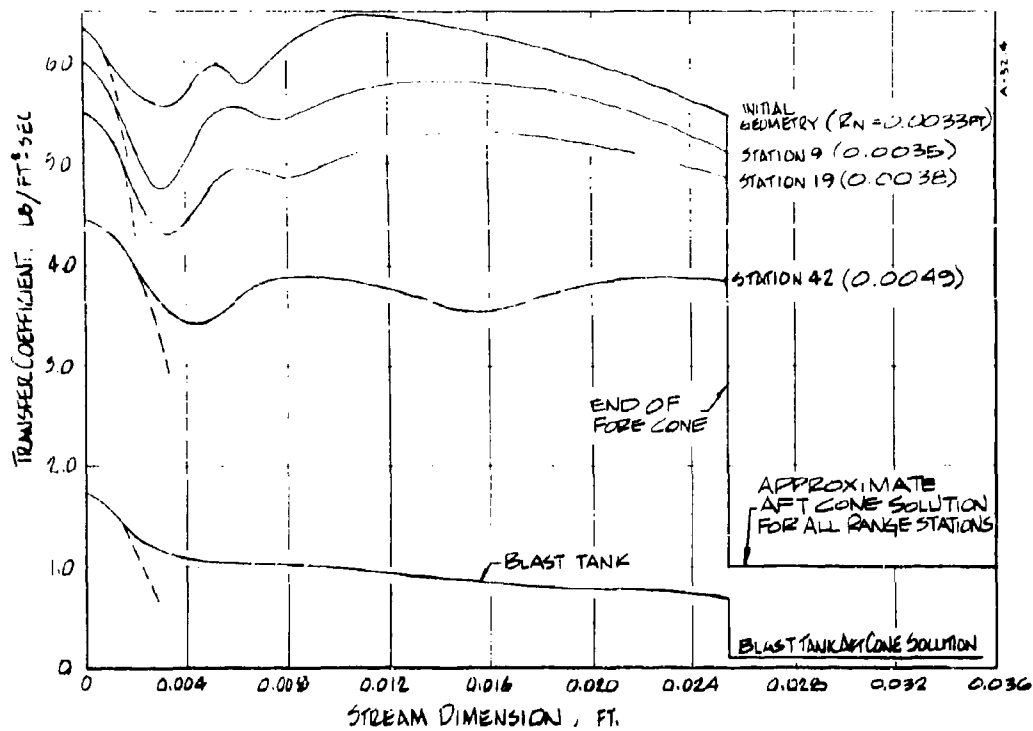
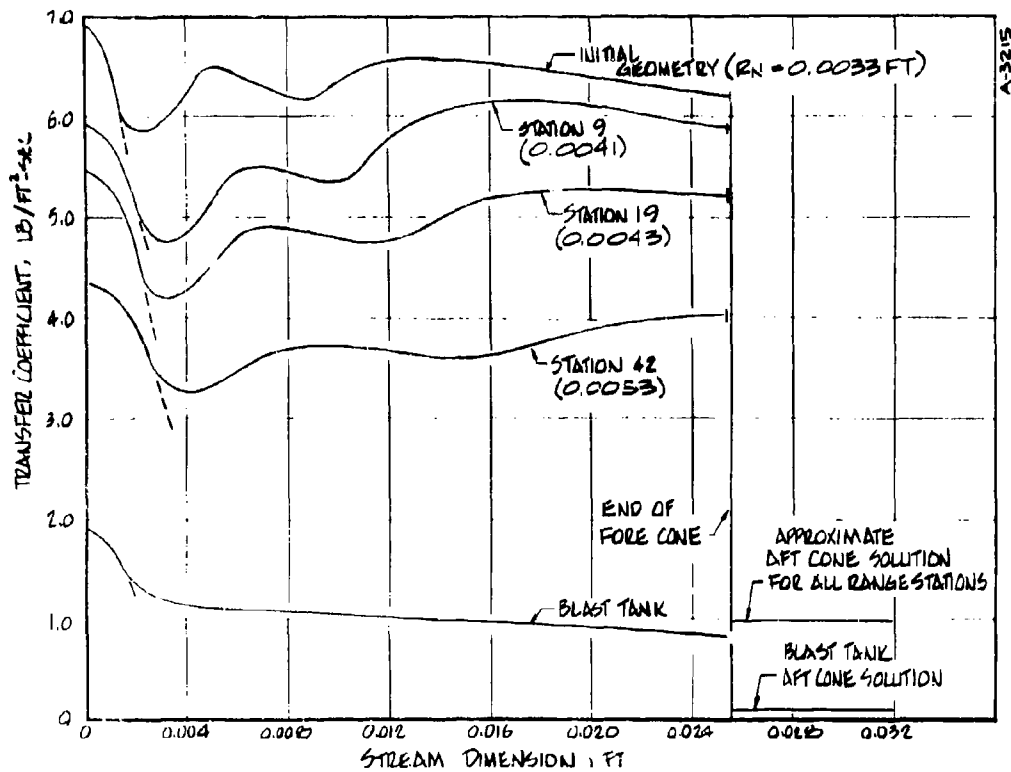


FIGURE 9 EFFECT OF BOUNDARY LAYER DEVELOPMENT  
ON VELOCITY PROFILES



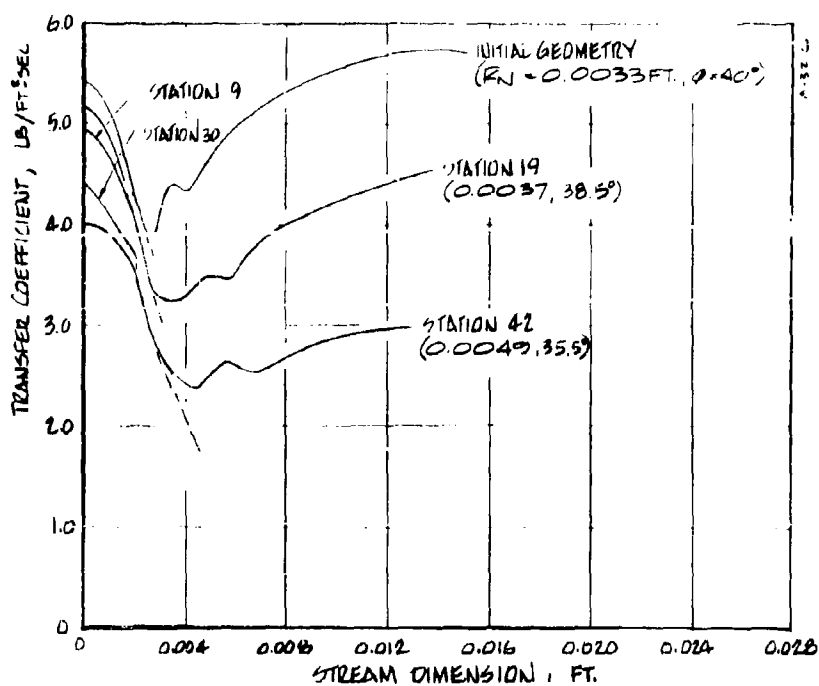
A) SHOT 1750 POLO GRAPHITE

FIGURE 10 PREDICTED TRANSFER COEFFICIENT DISTRIBUTIONS

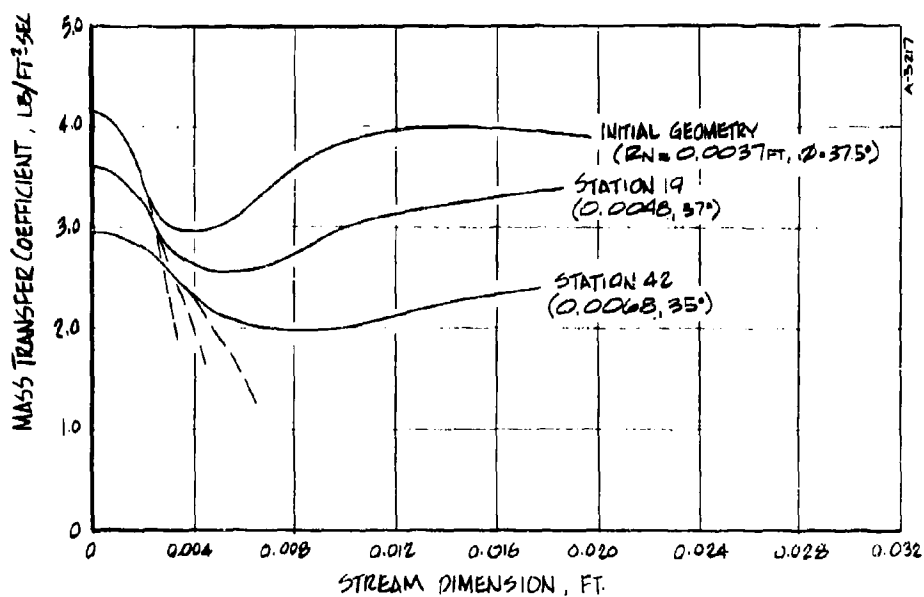


B) SHOT 1756 POLO GRAPHITE

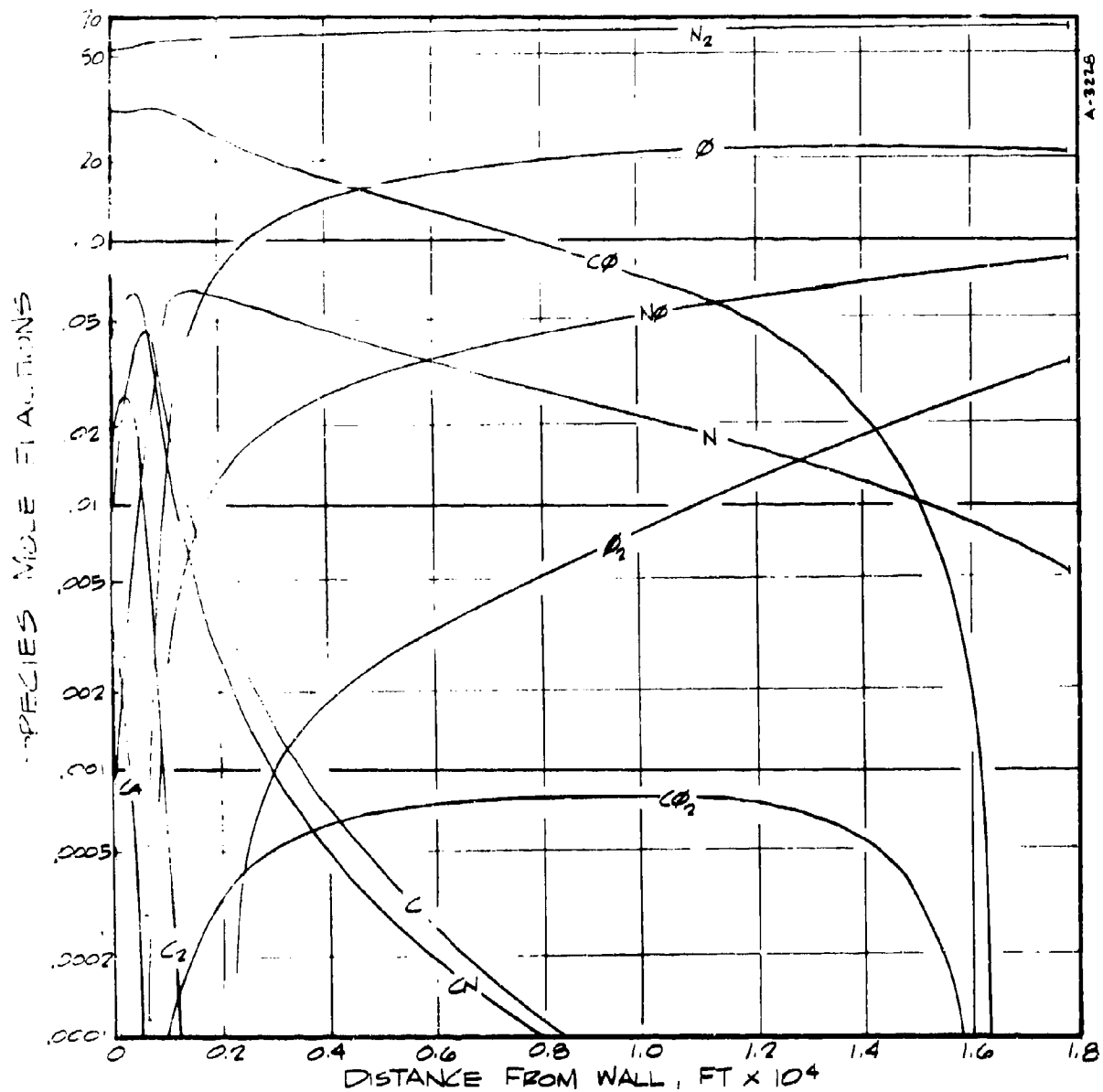
FIGURE 10, (CONTINUED)



C) SHOT 1763, R-6300, CARBON PHENOLIC  
FIGURE 10 (CONTINUED)

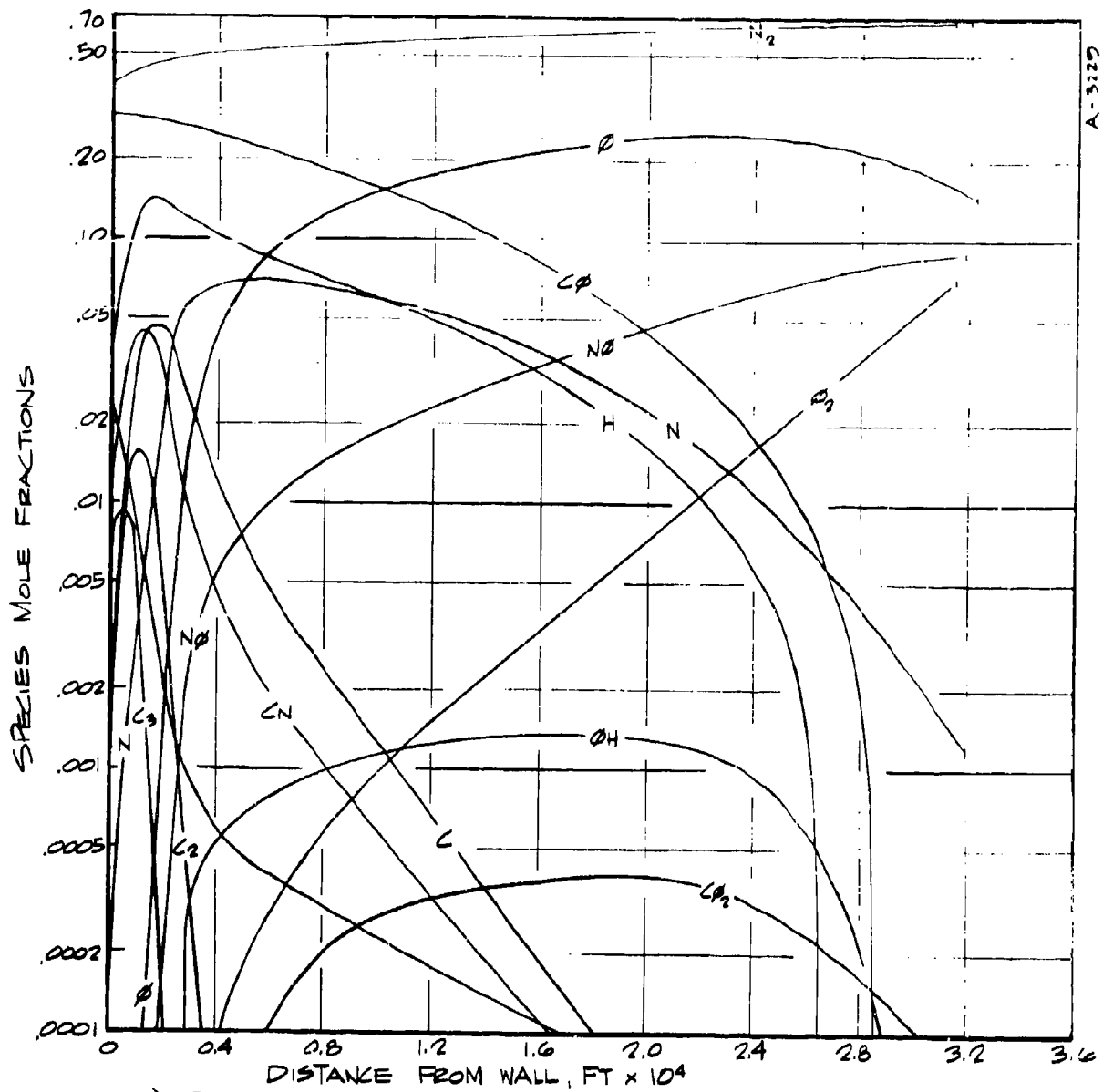


D) SHOT 1861, R-6300, CARBON PHENOLIC  
FIGURE 10 (CONCLUDED)



A) POCO GRAPHITE, SHOT 1756, STATION 9  $S/R_N = 2.0$

FIGURE 11 TYPICAL BOUNDARY LAYER  
COMPOSITION PROFILES



B) R6300 CARBON PHENOLIC, SHOT 1861, INITIAL GEOMETRY,  $S/R_N = 2.0$   
 FIGURE 11, (CONCLUDED)

#### 3.1.4 Comparison of Measured and Predicted Ablation Responses

The thermal and ablation response predictions for the two POCO graphite shots were performed by the ASTHMA code. The CMA code was utilized to compute the thermal and ablation response for two locations on each of the two R-6300 carbon phenolic models of interest. The ACE code was used to generate the equilibrium surface thermochemistry data required as input to both the CMA and ASTHMA codes. Plots of some of these data are given in Figure 12. Shown for the POCO graphite predictions are the normalized ablation rate versus surface temperature for various values of pressure. For the R-6300 carbon phenolic, normalized ablation rate versus surface temperature for various normalized pyrolysis gas rates at a particular pressure are shown.

Material thermal conductivity variations with temperature are given in Figure 13. The values used in the R-6300 predictions were those of a very similar material MX-4926 carbon phenolic at a  $0^\circ$  layup angle. Extrapolation to temperatures above  $8000^\circ\text{R}$  was required.

Various results of the transient thermal response predictions are given in Figures 14 through 16. Figure 14 shows the variations of surface temperature at various locations on the respective models. Also shown as symbols are various steady state surface temperatures computed by the BLIMP code. This comparison verifies that essentially steady state ablation occurs throughout the ballistic range shots.

Figure 15 gives several typical predicted in-depth temperature and, for the R-6300 carbon phenolic, density profiles at the last measurement station. The figure indicates that the back wall temperatures in the POCO graphite models are high enough to cause the epoxy bonds and Scotchply backup to begin decomposing ( $\sim 1000^\circ\text{R}$ ). Heat soak did not reach the back surface of the R-6300 models, however.

The predictions of nose region recession for the four shots are shown in Figure 16. Comparison is made between the final measured geometries and the predicted surface locations data points. For shot 1750, an additional prediction which accounts for thermal expansion is shown. This prediction will be discussed in the following section. In general, less ablation was predicted than was indicated by the in-flight model photographs. At the stagnation point for all cases, predicted recession was about  $1/3$  of measured, while on the cone region, predicted was only about  $1/2$  of measured.

#### 3.1.5 Thermal Expansion Calculations

Two elastic thermal expansion calculations were made utilizing the DOASIS code described in Section 2. The ASTHMA prediction of shot 1750 provided the

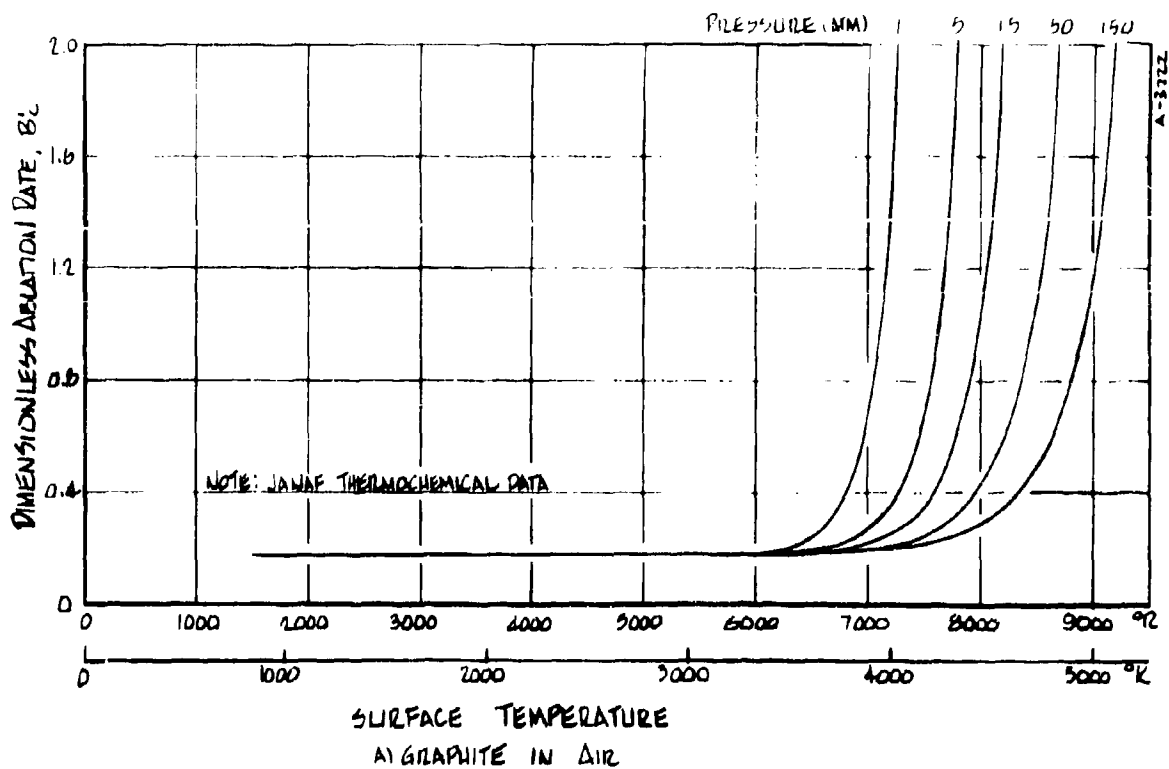


FIGURE 12, EQUILIBRIUM SURFACE THERMOCHEMICAL ABLATION DATA

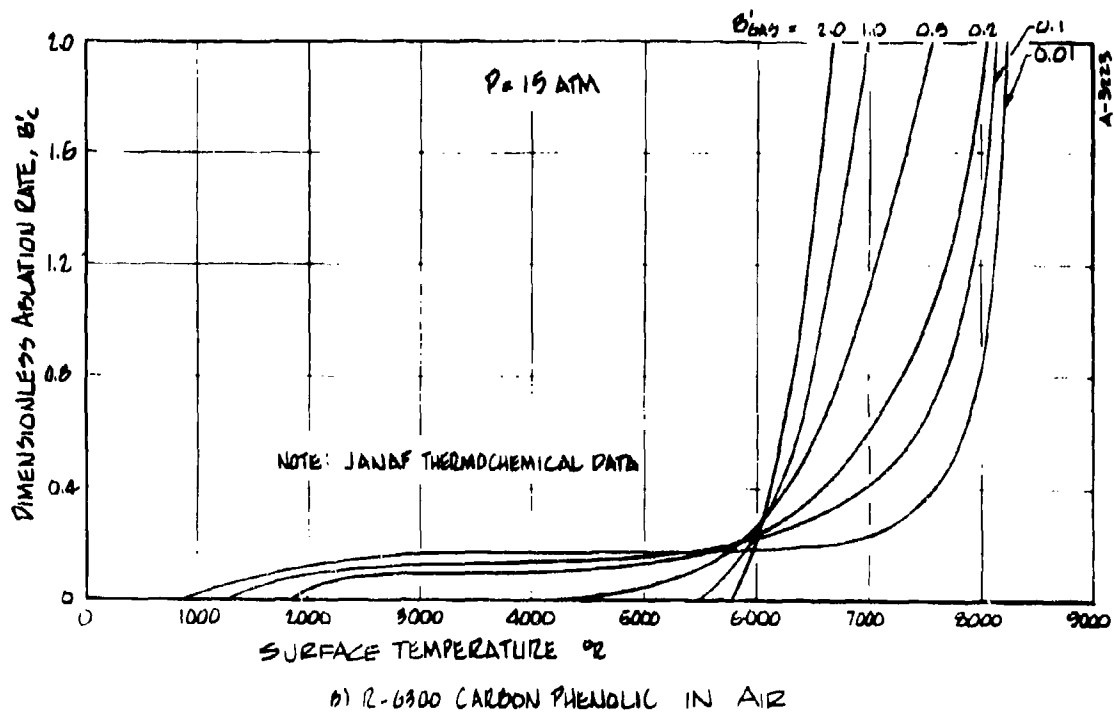
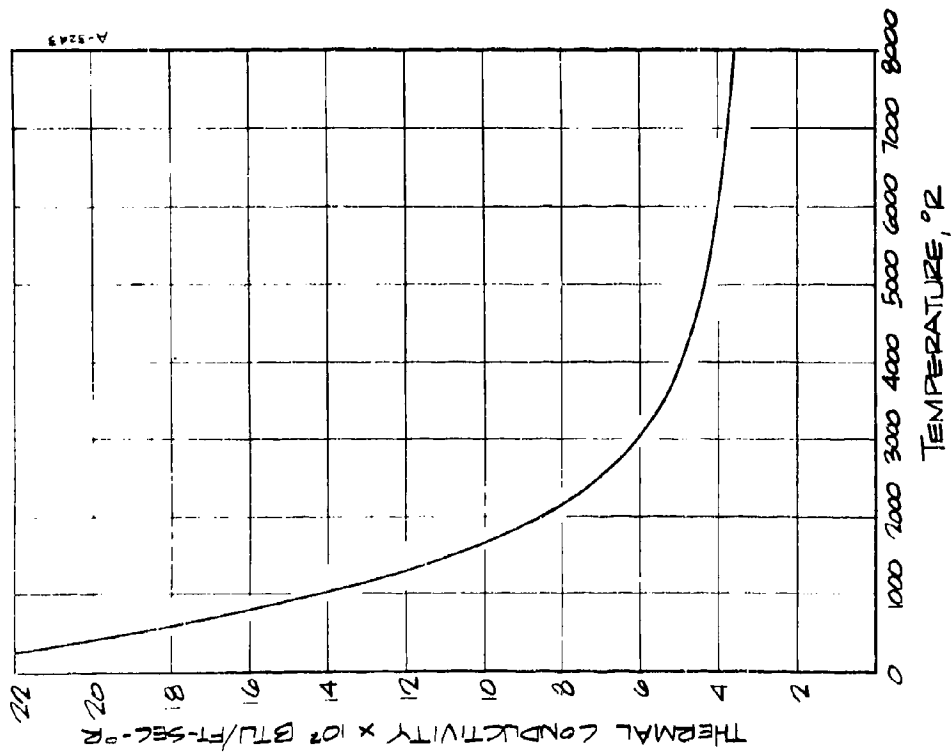
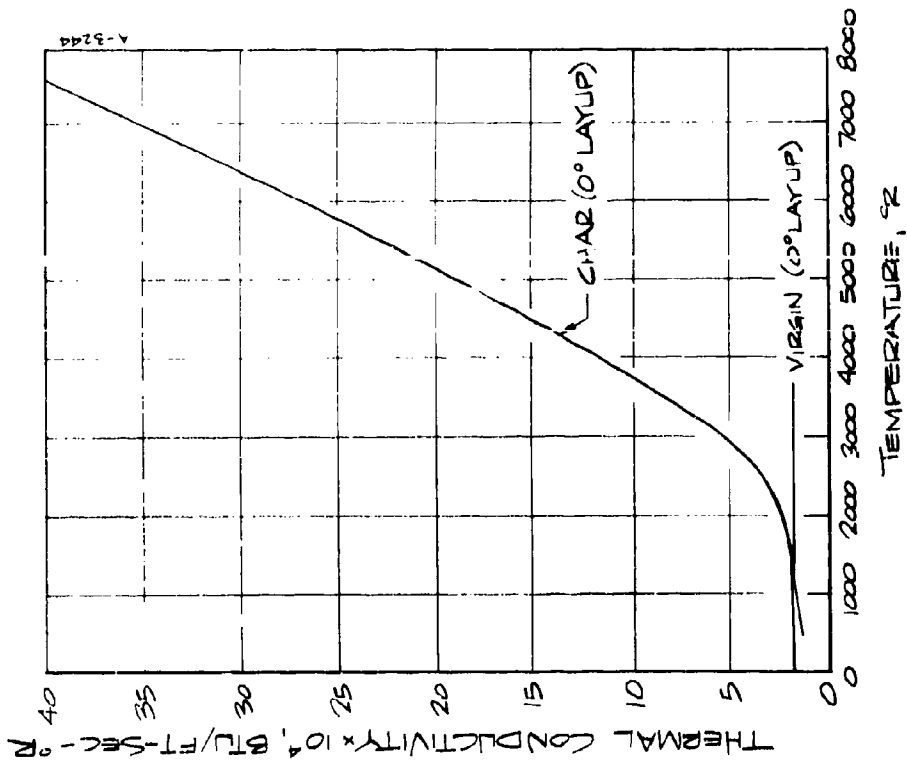


FIGURE 12 (CONCLUDED)

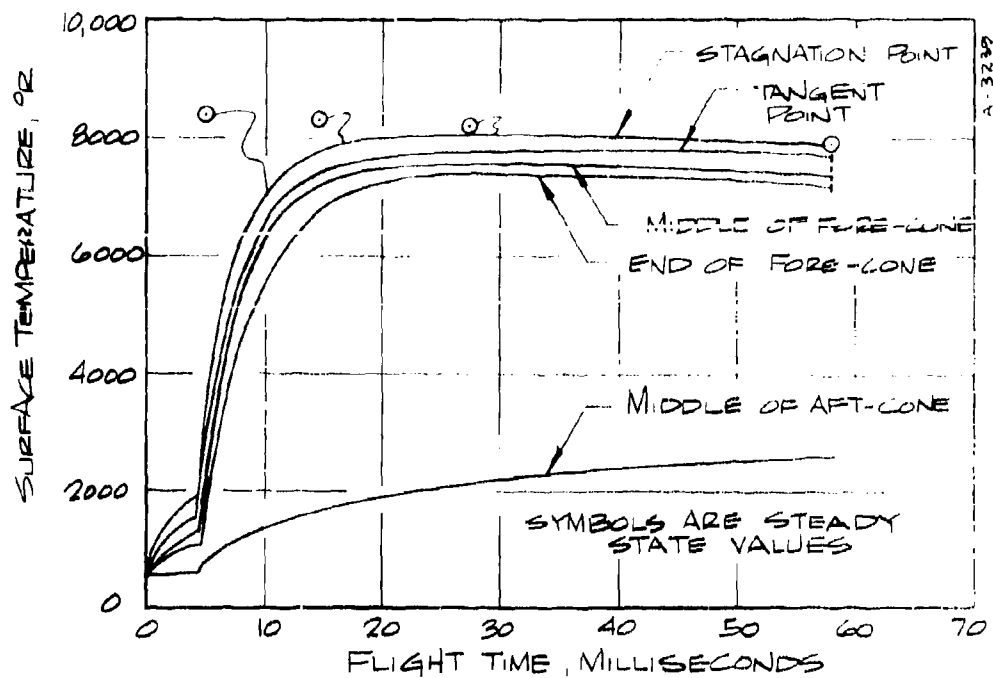




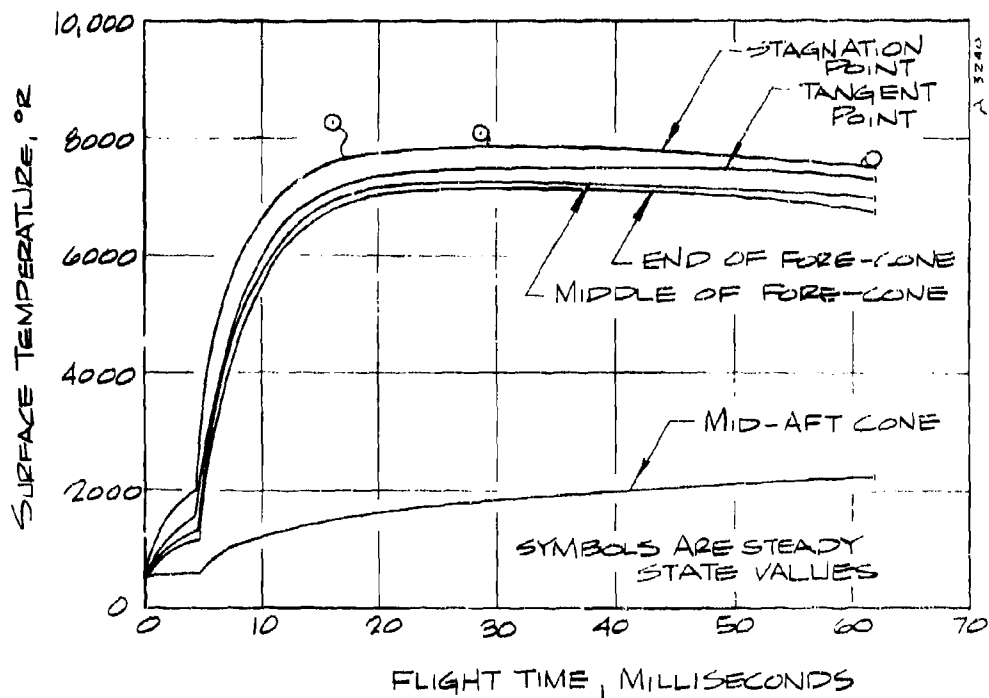
A) POCO GRAPHITE  
FIGURE 13 MATERIAL THERMAL  
CONDUCTIVITY DATA



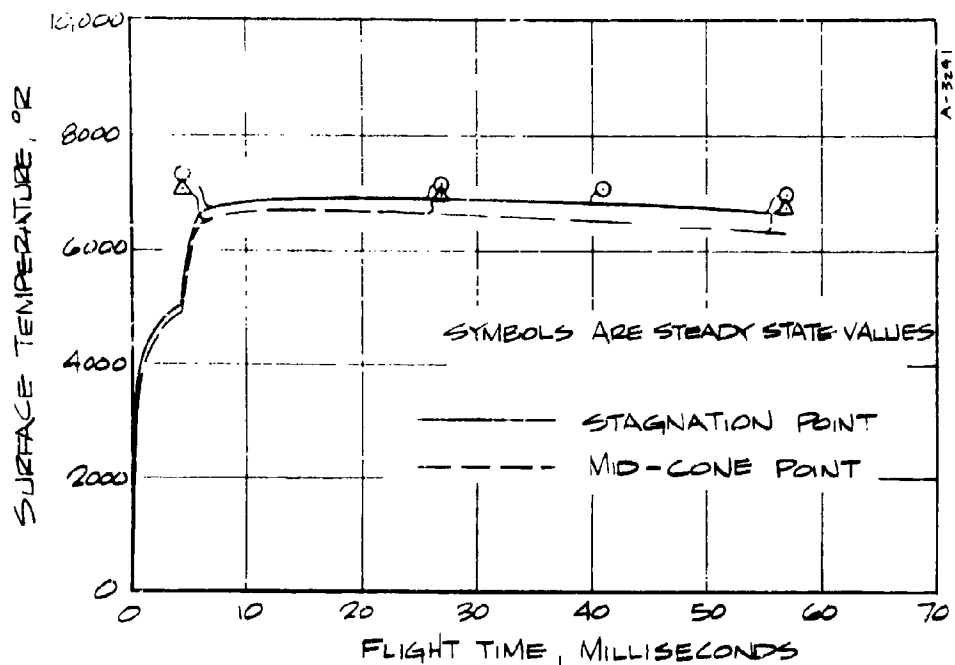
B) CARBON PHENOLIC DATA  
FIGURE 13. (CONCLUDED)



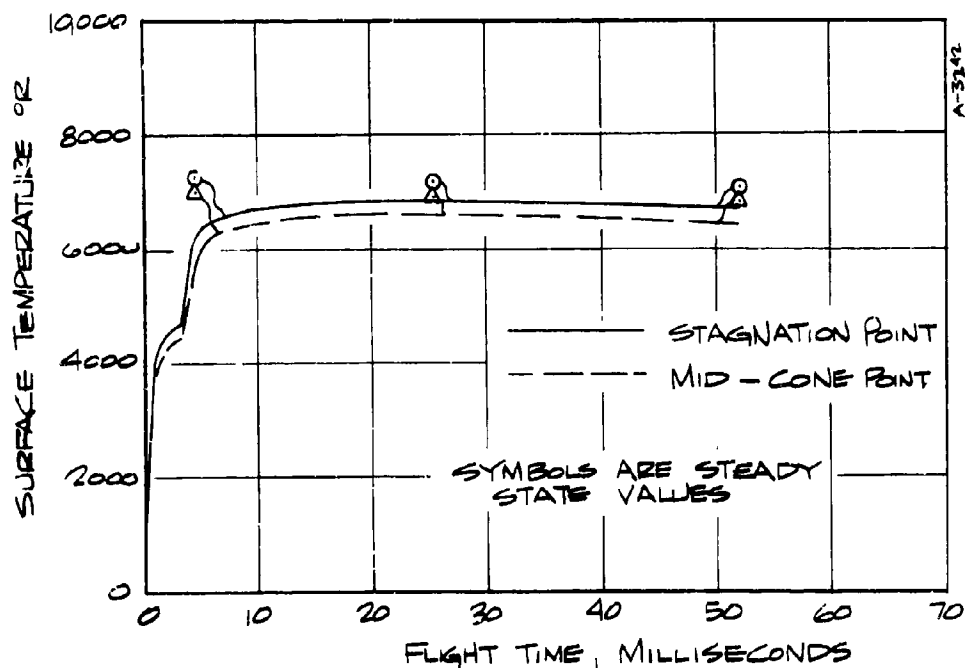
A) SHOT 1750, POLO GRAPHITE  
 FIGURE 14, PREDICTED SURFACE TEMPERATURE HISTORIES



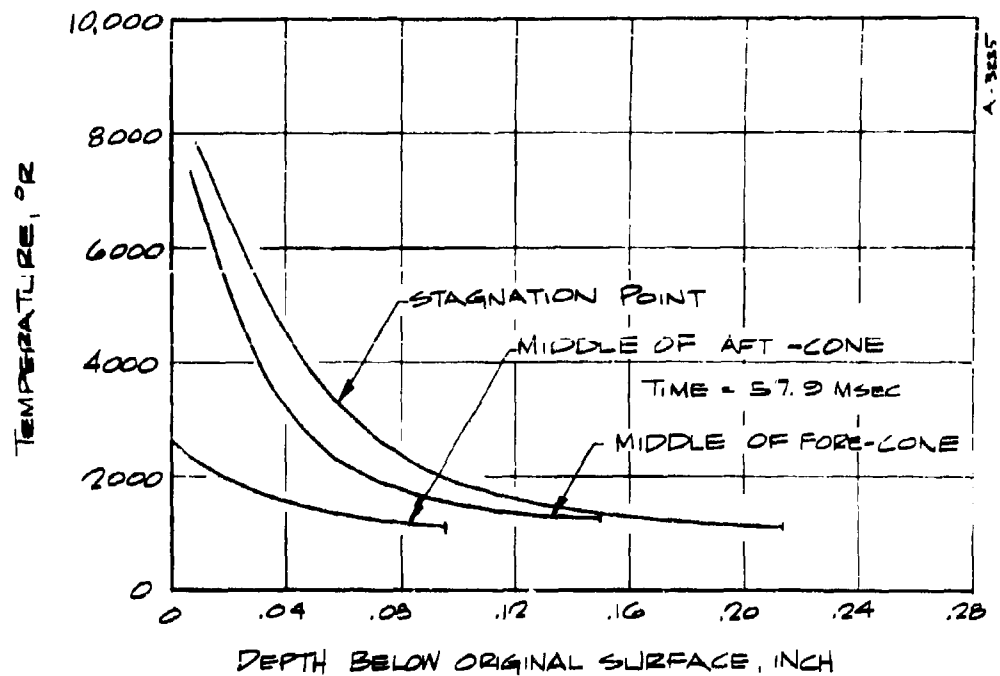
B) SHOT 1756, POLO GRAPHITE  
 FIGURE 14, (CONTINUED)



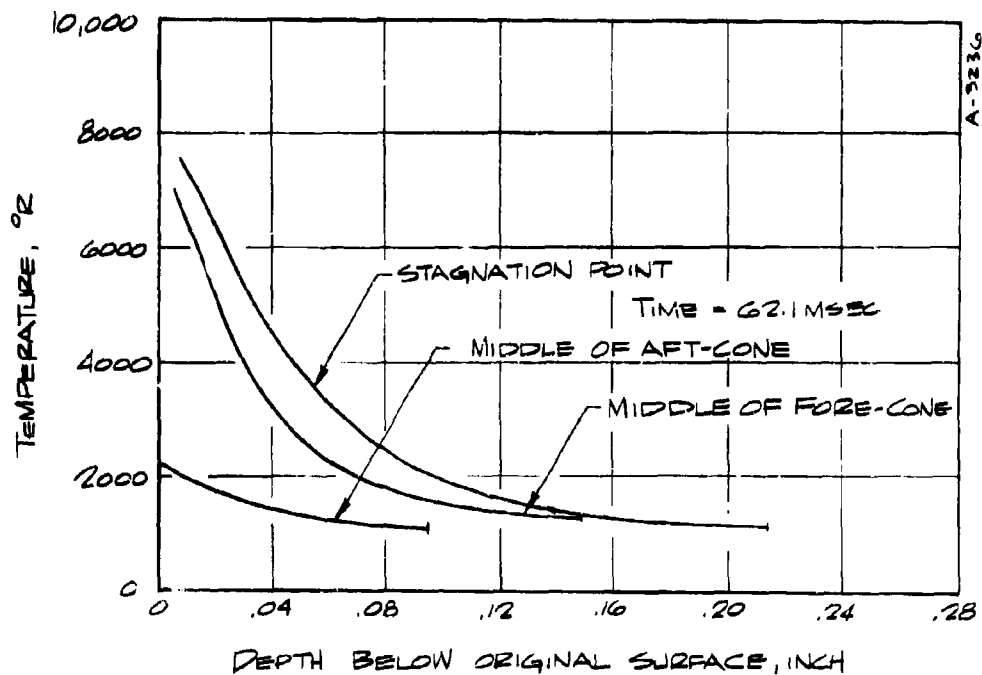
C) SHOT 1763, R6300 CARBON PHENOLIC  
FIGURE 14 (CONTINUED)



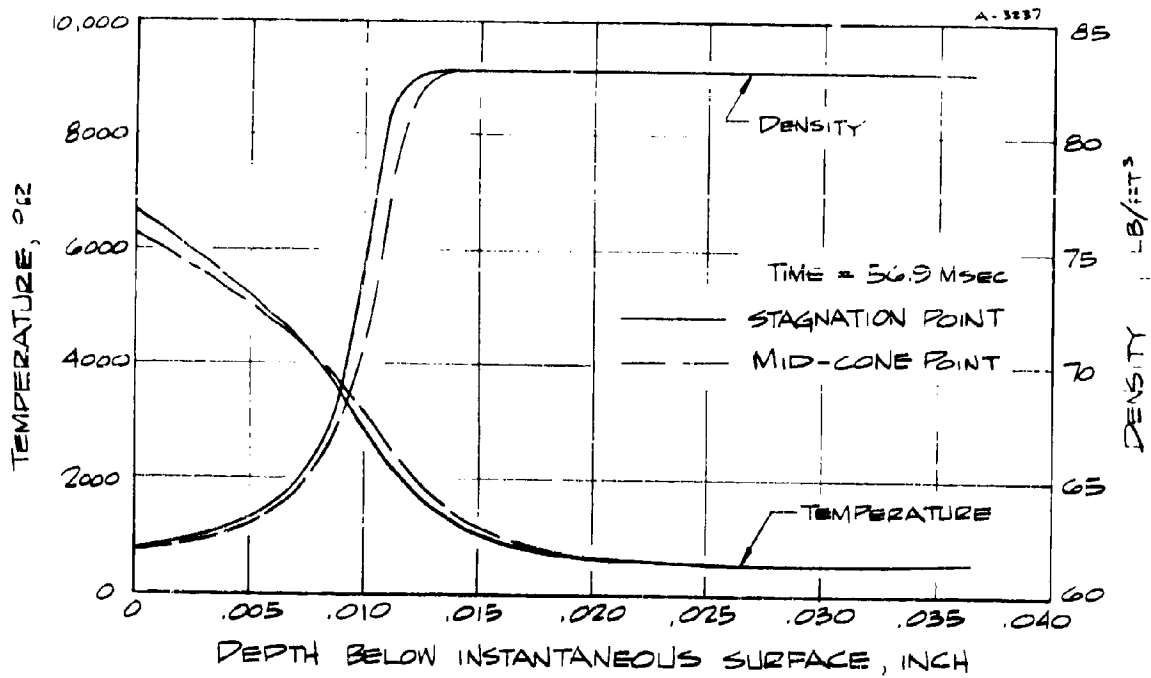
D) SHOT 1861, R6300 CARBON PHENOLIC  
FIGURE 14, (CONCLUDED)



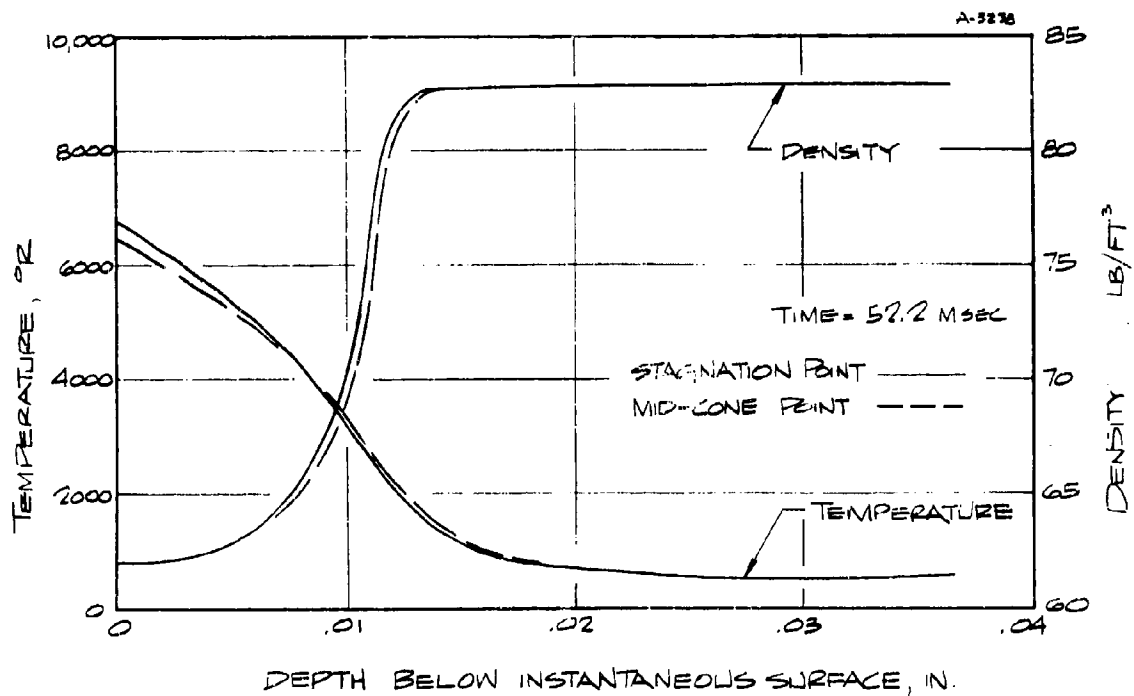
A) SHOT 1750, POCO GRAPHITE  
FIGURE 15 IN-DEPTH THERMAL RESPONSES



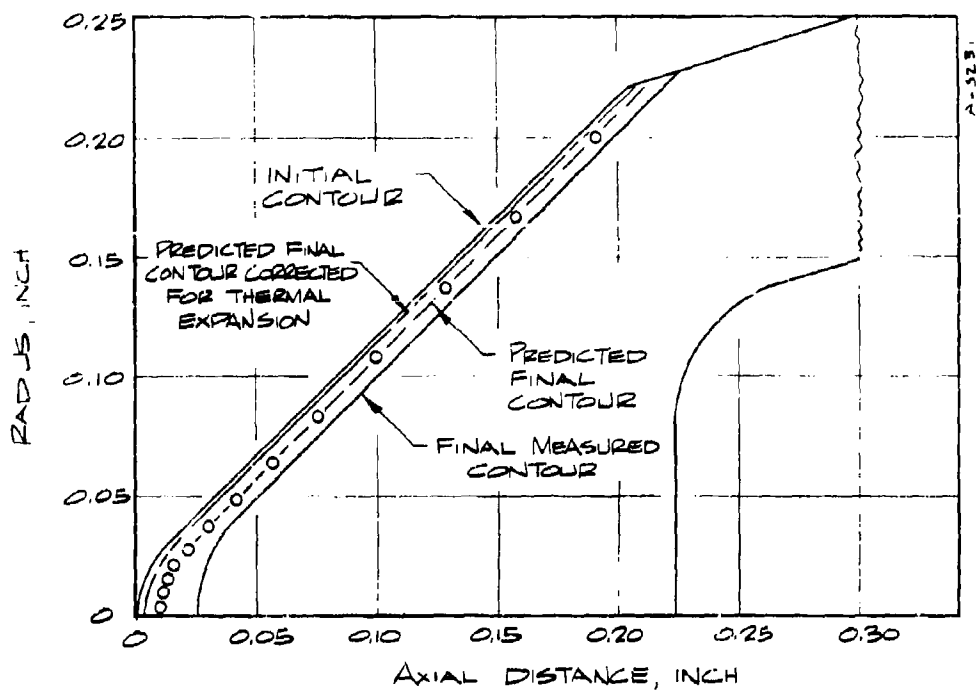
B) SHOT 1756, POCO GRAPHITE  
FIGURE 15, (CONTINUED)



C) SHOT 1763, R6300 CARBON PHENOLIC  
FIGURE 15 (CONTINUED)

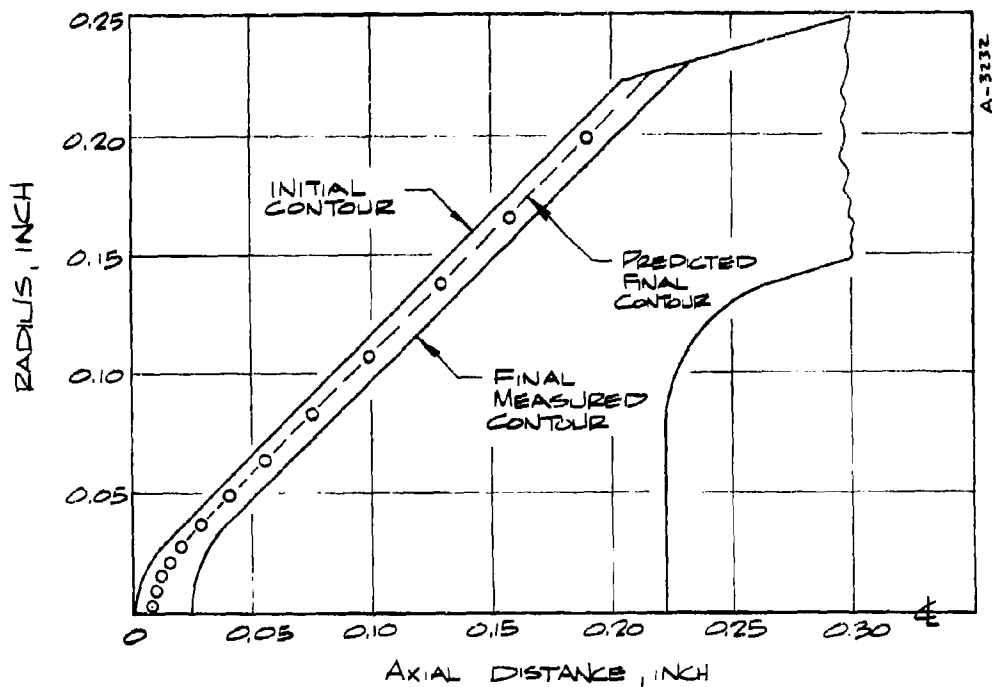


D) SHOT 1861, R6300 CARBON PHENOLIC  
FIGURE 15 (CONCLUDED)



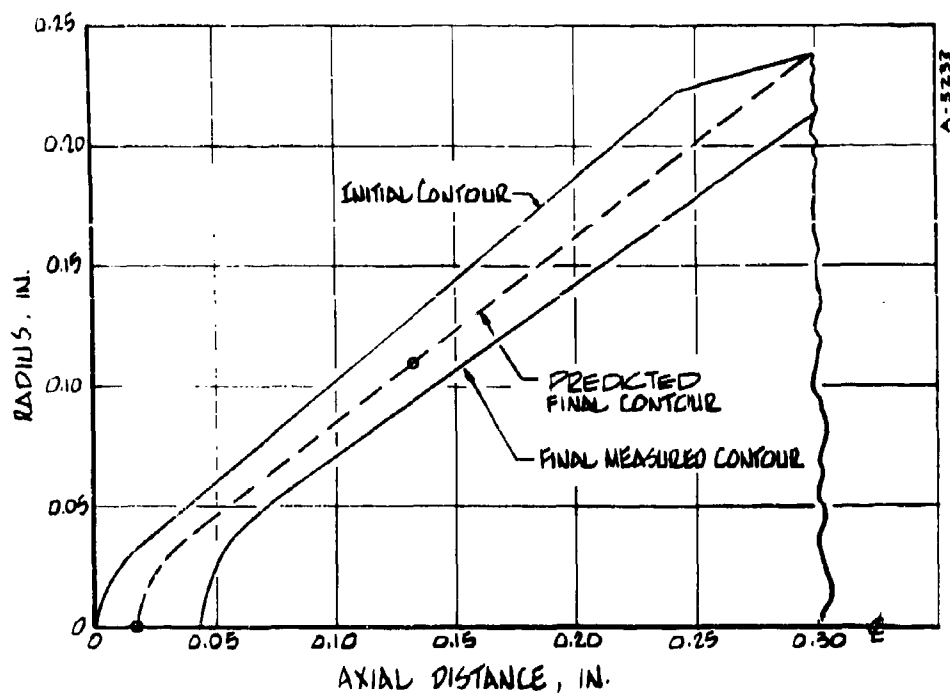
A) SHOT 1750, POCO GRAPHITE

FIGURE 16 COMPARISON OF PREDICTED AND MEASURED MODEL RECESSION



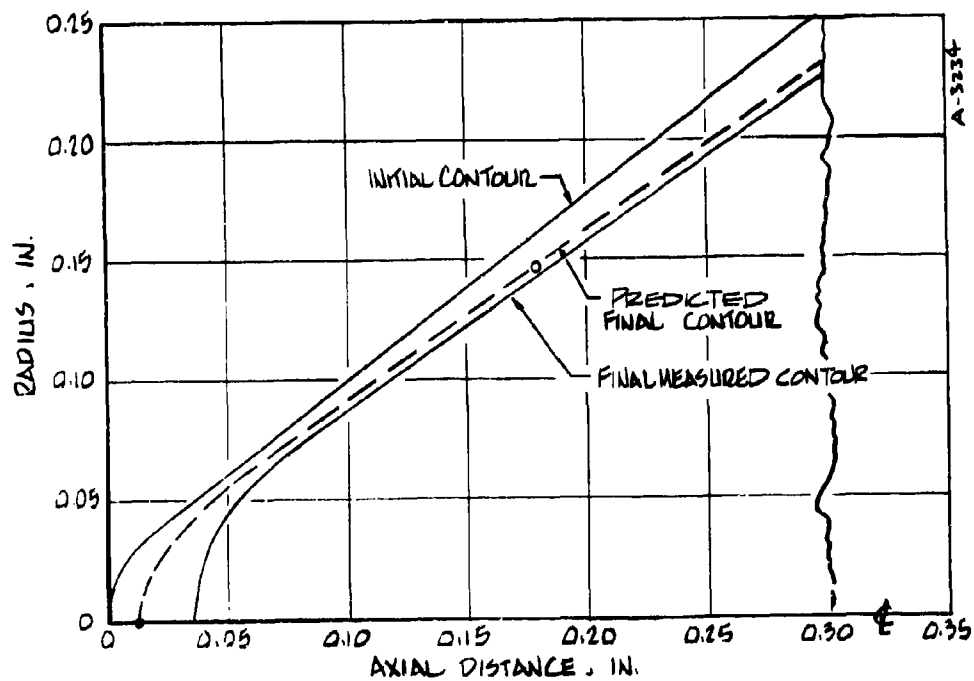
B) SHOT 1756, POCO GRAPHITE

FIGURE 16 (CONTINUED)



C) SHOT 1763, R-6300 CARBON PHENOLIC

FIGURE 16 (CONTINUED)



D) SHOT 1861, R-6300 CARBON PHENOLIC

FIGURE 16 (CONCLUDED)

necessary thermal and mechanical loading plus the geometrical input data. The finite element network and temperature distributions employed are shown in Figures 17a and b respectively. Thermal-structural properties of the POCO graphite were obtained from Reference 24. Predictions were made for two back wall support conditions. These were:

- Nose tip supported by Scotchply plug on the back wall (Surface A in Figure 1)
- Nose tip supported by beryllium-copper afterbody at the end of the aft-cone (Surface B in Figure 1)

The second condition more accurately represents the actual support condition for shot 1750. For comparison purposes, both cases were run. For the support at surface A, the thermal expansion at the stagnation point was 2.5 mils and less than 1 mil at the bi-conic intersection. For the support at surface B, the thermal expansion was 6.5 mils at the stagnation point and 4.0 mils at the bi-conic intersection. The differences between these two surfade expansions comes from the differential thermal expansion between support A and B. Figure 16a shows the predicted final contour corrected for the latter thermal expansion.

Sufficient high temperature material properties data was not available to adequately perform a reliable plasticity analysis, however, it should be pointed out that inclusion of plastic flow at the outer surface ( $T > 5000^{\circ}\text{F}$ ) would decrease the predicted thermal expansion. Consequently, the thermal expansion shown in Figure 16a should be considered as an upper limit.

### 3.2 WAVE SUPERHEATER AND 50 MW RENT FACILITY TESTS

Calculations presented above for ballistic range tests required consideration of the changing free stream conditions and to some extent, changing model contour with time. The wave superheater and RENT facility tests are characterized by only minor changes in test conditions with time and the particular test models chosen for analysis were selected on the basis of having established a relatively stable shape. Because of the high convective heating rate conditons, it is reasonable to assume that steady state energy and mass balances at the surface are representative of reality for test times of approximately 1 second and longer. Hence, for each model analyzed an ablation prediction was performed for one point in time. The test conditions and model contours are described first, in Section 3.2.1, and are followed by a description of inviscid flow representation and boundary layer solutions in Sections 3.2.2 and 3.2.3 respectively. Predicted ablation response and comparison to data are given in Section 3.2.4.



A) NODAL NETWORK  
FINITE ELEMENT ANALYSIS OF BALLISTIC  
RANGE POCO MODEL (TEST NO. 1750)

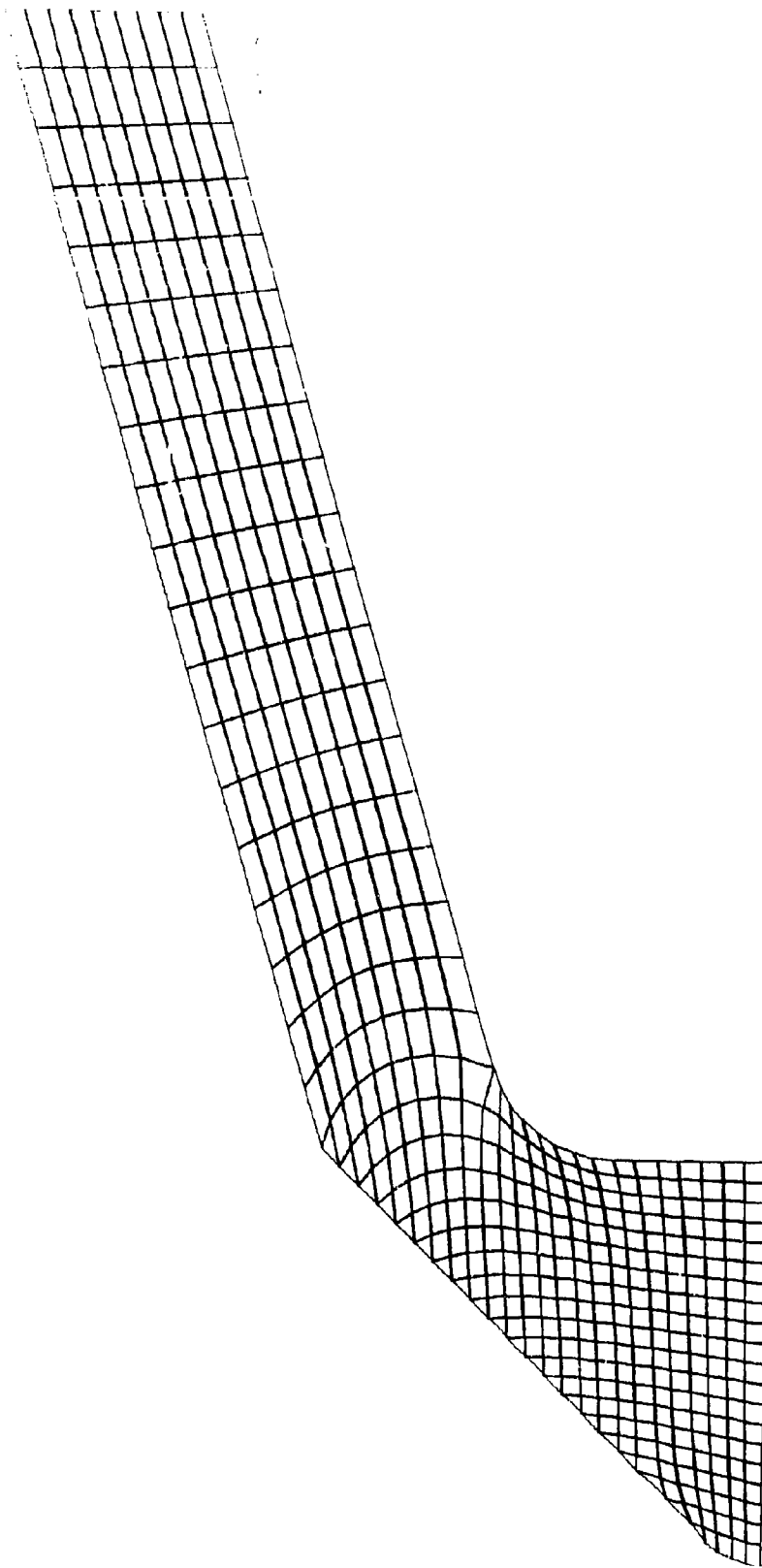
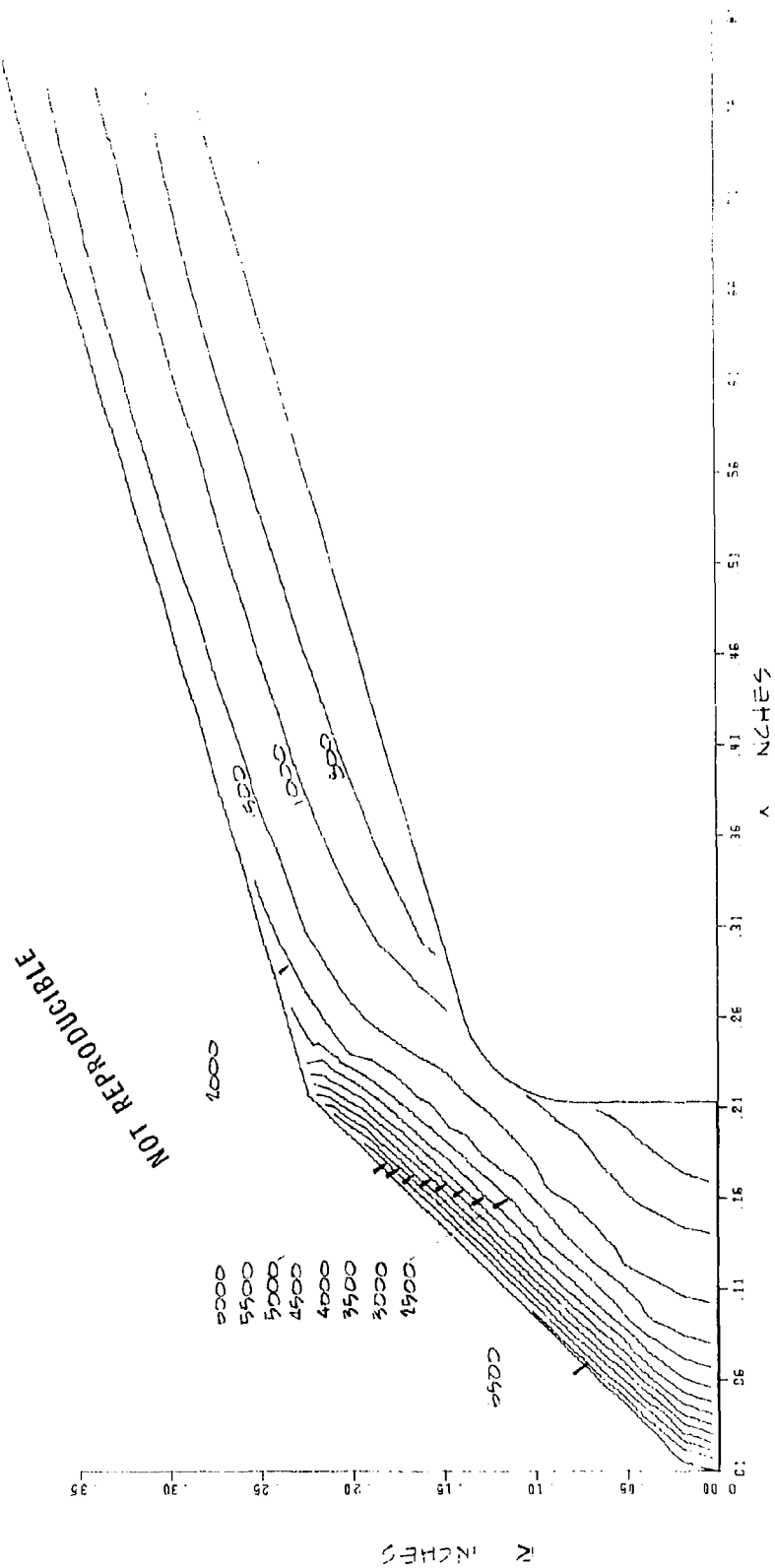


FIGURE 1. CONTINUED

8. TEMPERATURE DISTRIBUTION AT 60 MILLISECONDS



### 3.2.1 Test Conditions and Model Contours

For the models tested in the WSH, the stagnation point impact pressure ( $P_{t_2}$ ) and total enthalpy ( $H_0$ ) values used in the calculations were taken directly from Reference 1. The enthalpy values reported in Reference 1 were decreased by 129. Btu/lbm to be consistent with the JANAF enthalpy base state employed here.

For the models tested in the RENT facility, the stagnation point pressures used in the analyses accounted for the flight impact pressure decay along the stream centerline. At a given axial location the impact pressure was obtained from the measured chamber pressure (Ref. 3) and the ratio of impact to chamber pressure shown in Figure 18 taken from the measurements reported in Reference 25. The bulk stream enthalpy values for the models tested in the RENT facility are reported in Reference 3. However, calorimetric heat flux measurements reported in References 25 and 26 indicate that there is a significant centerline "heat flux spike" in the RENT test jet at high pressure conditions. Centerline enthalpy measurements have not yet been made for the RENT test jet although heat flux measurements and heat transfer calculations in Reference 25 suggest that the high centerline heat flux results because the centerline enthalpy is on the order of 5000 Btu/lbm for the 2400 Btu/lbm nominal bulk enthalpy high pressure test conditions. Also, the studies of Reference 27 demonstrate that the model response is essentially unaffected by the enthalpy of the fluid away from the vicinity of the centerline provided the ablation model is aligned with the enthalpy spike. It stands to reason that a misalignment would result in an asymmetric ablation contour and this was not observed for the models that were analyzed. Thus, ablation response calculations for models tested in the RENT facility utilized an enthalpy of 5000 Btu/lbm. To assess the affect of this enthalpy uncertainty, an additional calculation was carried out using the reported bulk enthalpy, and this is discussed in Section 3.2. The test conditions considered for each model analyzed are listed in Table II.

The model contour histories obtained from the movie film data and the contours analyzed are shown in Figures 19a through e. The film data was obtained from References 1 and 3 and the model contours were selected to represent an average effective axisymmetric steady state shape. Figures 20a through e present measured surface recession as a function of time for all models. Also shown in these figures are the effective cone half angle and nose radii as deduced from the film data for all models except model 12-2 which did not assume a bi-conic shape. For models tested in the wave superheater the measured stagnation point surface temperature history is also shown. By way of example, the method employed to select the time at which analyses were

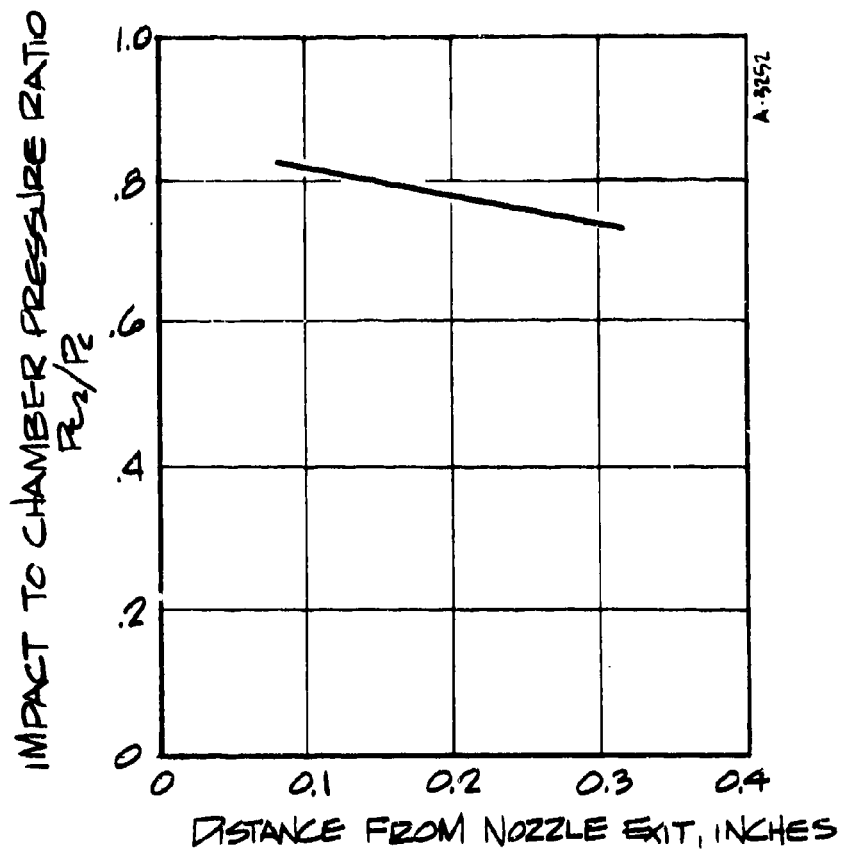
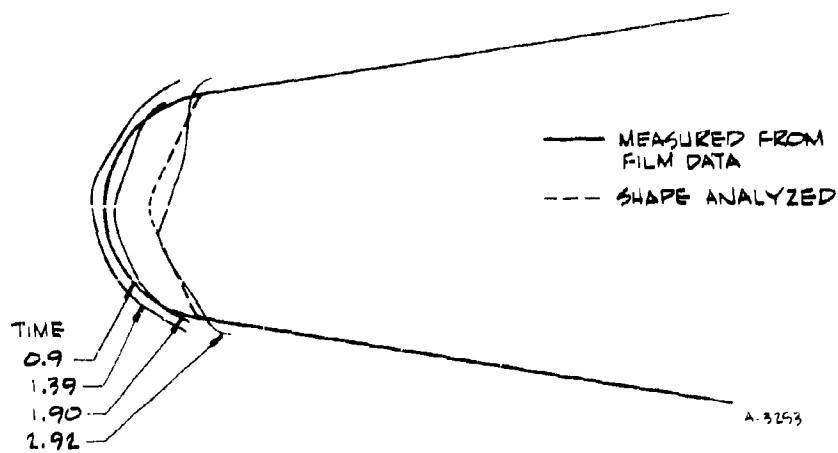


FIGURE 18 STREAM CENTERLINE  
IMPACT PRESSURE DECAY  
WITH AXIAL DISTANCE

TABLE II

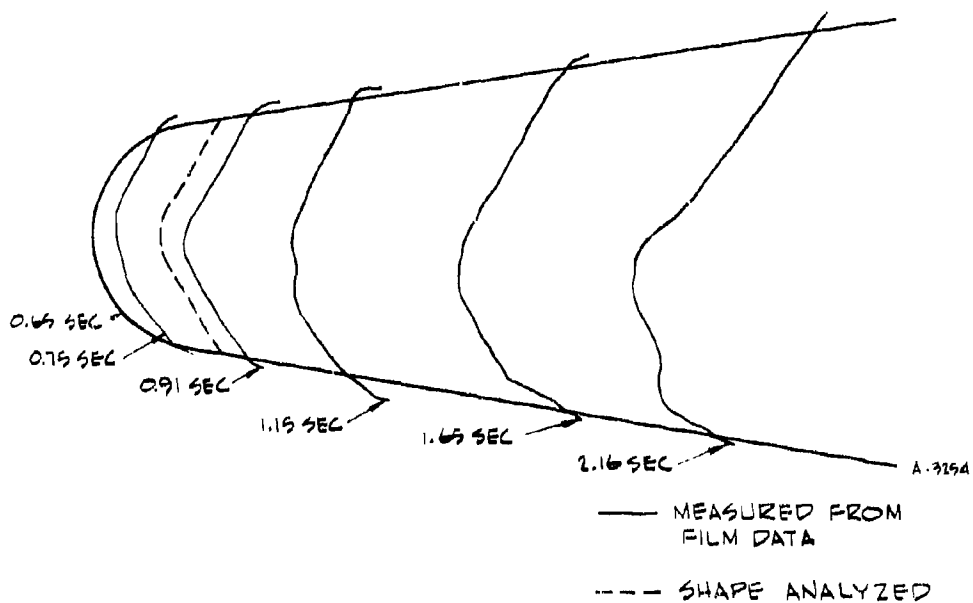
## TEST CONDITIONS FOR WAVE SUPERHEATER AND RENT TESTS

MODEL NO.	TEST NO.	FACILITY	MATERIAL	$P_{t2}$ (atm)	$H_0$ (Btu/lb)	TIME AT WHICH MODEL RESPONSE ANALYZED (sec)	ADLATED NOSE GEOMETRY (From Film Data)
C-9	69-281	WSH	POCO Graphite	78.	2103.	2.8	Bi-Conic; 64° cone half-angle
CP-16	70-008	WSH	R-6300 Carbon Phenolic	103	2164	0.9	Bi-Conic; 60° cone half-angle
12-2	14-5	50 MW	POCO Graphite	77.	5000		Blunted "laminar" shape
103A	14-3	50 MW	R-6300 Carbon Phenolic	57	5000	0.7	Bi-Conic; 43° cone half-angle
123A	14-4	50 MW	R-6300 Carbon Phenolic	77	5000	0.6	Bi-Conic; 43° cone half-angle



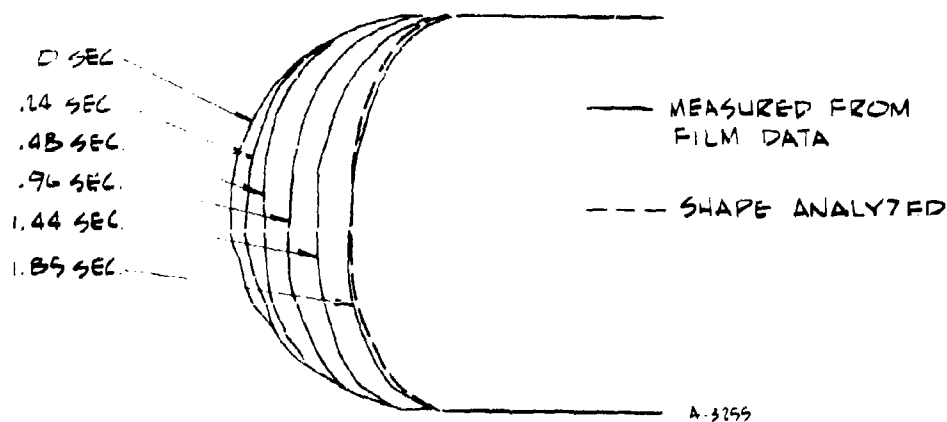
A) POCO GRAPHITE (MODEL G-9) WAVE SUPERHEATER

FIGURE 19. ABLATED NOSE CONTOUR FROM FILM DATA AND NOSE GEOMETRY EMPLOYED IN THE ANALYSIS



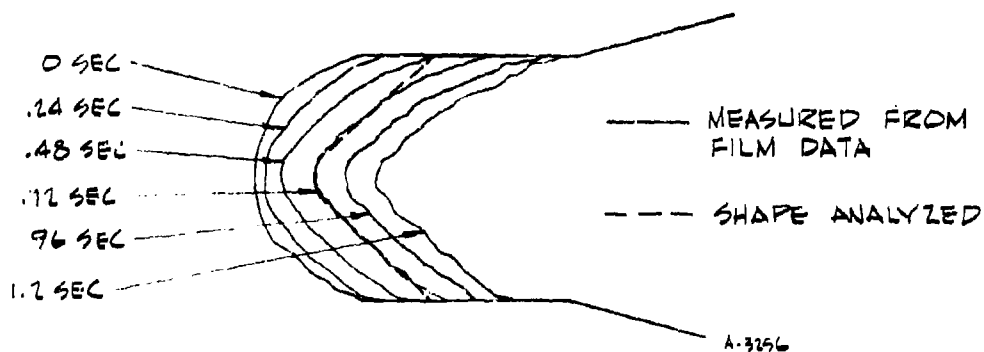
B) R-6300 CARBON PHENOLIC (MODEL CP-16) WAVE SUPERHEATER

FIGURE 19 CONTINUED



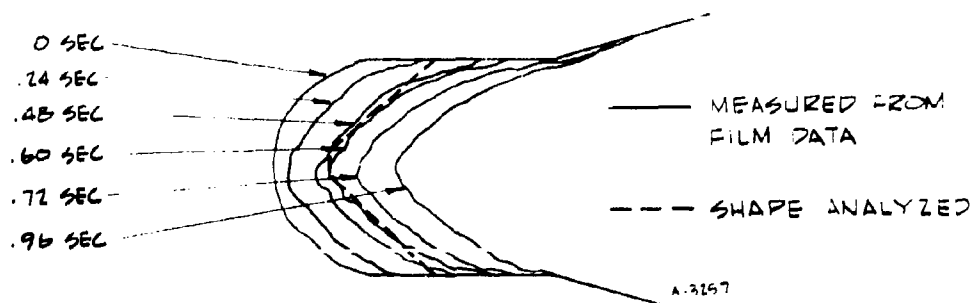
C) POLO GRAPHITE (MODEL 12-2) RENT

FIGURE 19. CONTINUED



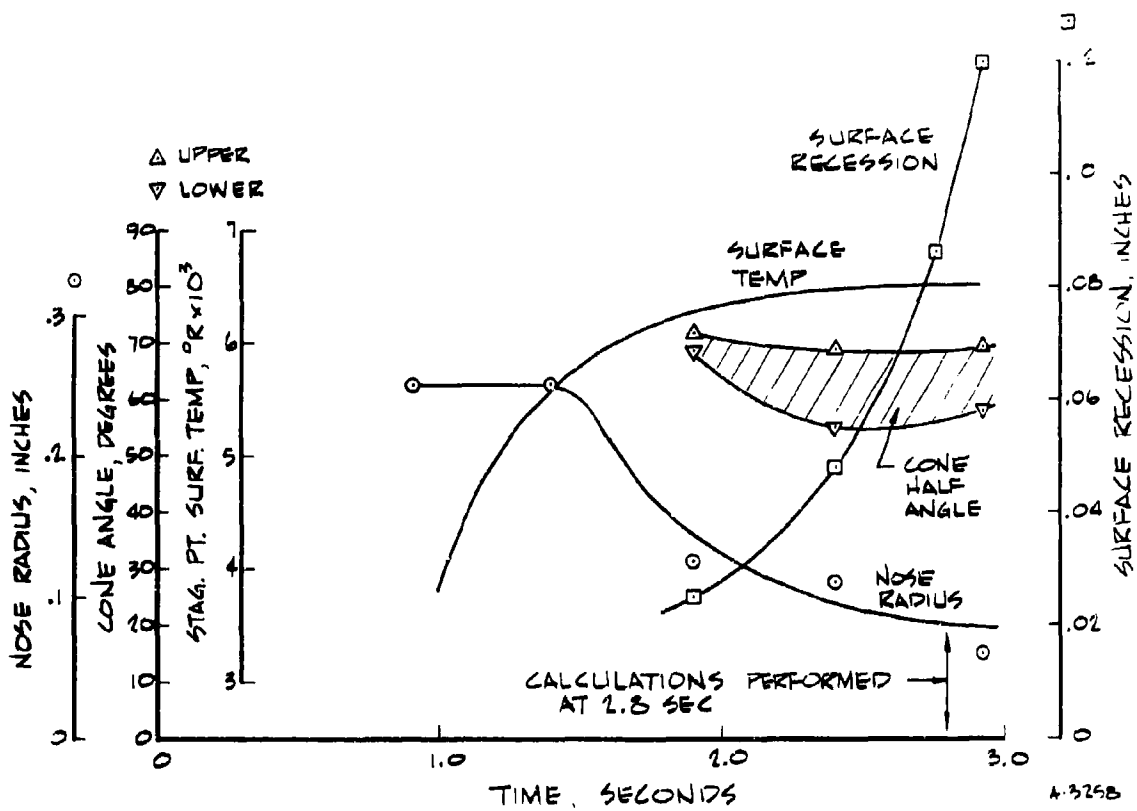
D) R-6300 CARBON PHENOLIC (MODEL 103A) RENT

FIGURE 19. CONTINUED



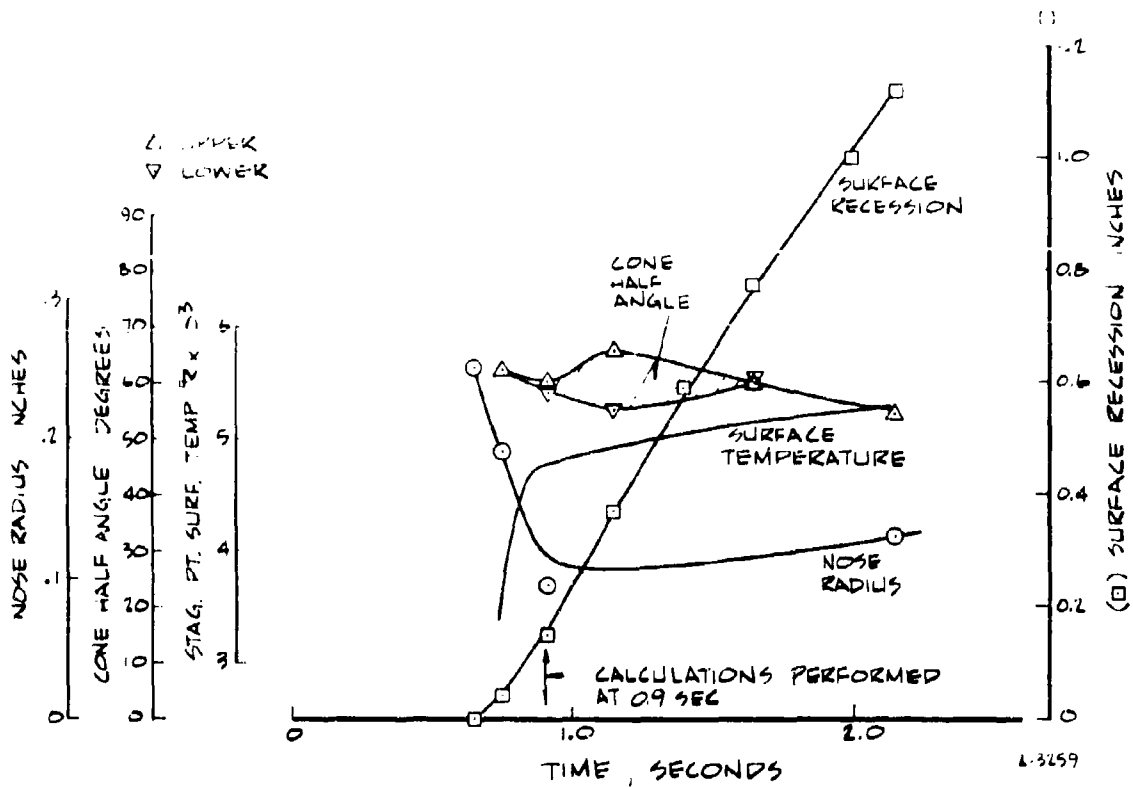
E) R-6300 CARBON PHENOLIC (MODEL 123A) RENT

FIGURE 19 CONCLUDED



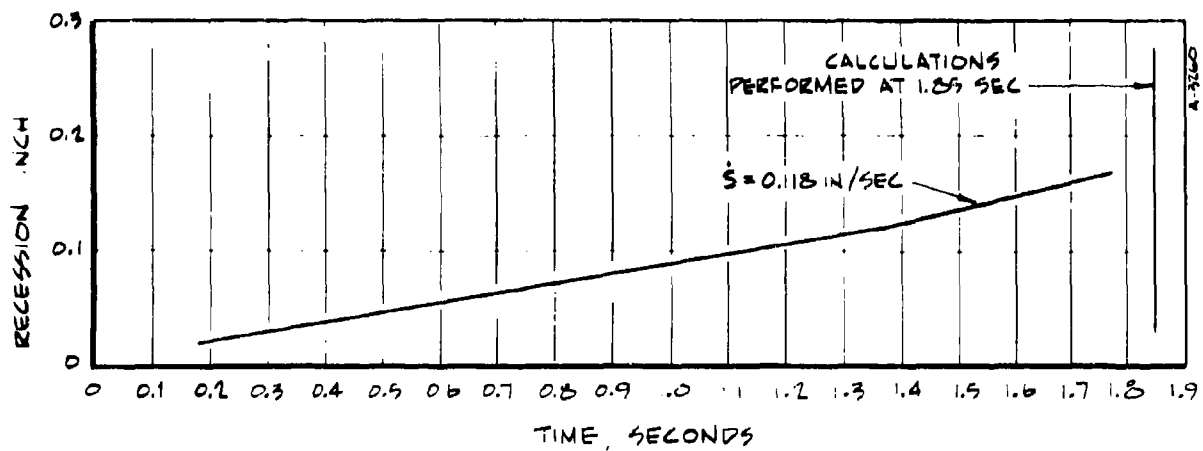
A) POLO GRAPHITE (MODEL G-9) WAVE SUPERHEATER  
CONTOUR AT 2.8 SECONDS  $\theta_c = 64^\circ$   $R_N = 0.020$  IN





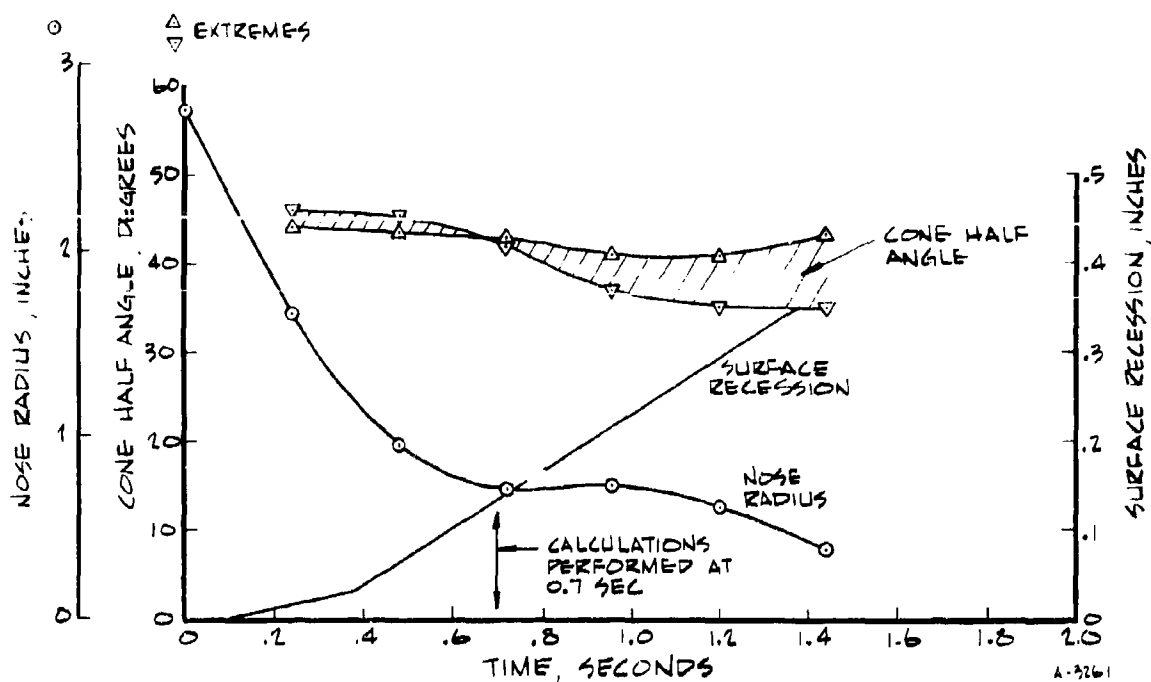
B) R-6300 CARBON PHENOLIC (MODEL CP-16) WAVE SUPERHEATER  
 CONTOUR AT 0.9 SECONDS,  $\theta_c = 60^\circ$ ,  $R_N = 0.12$  IN.

FIGURE 20 CONTINUED



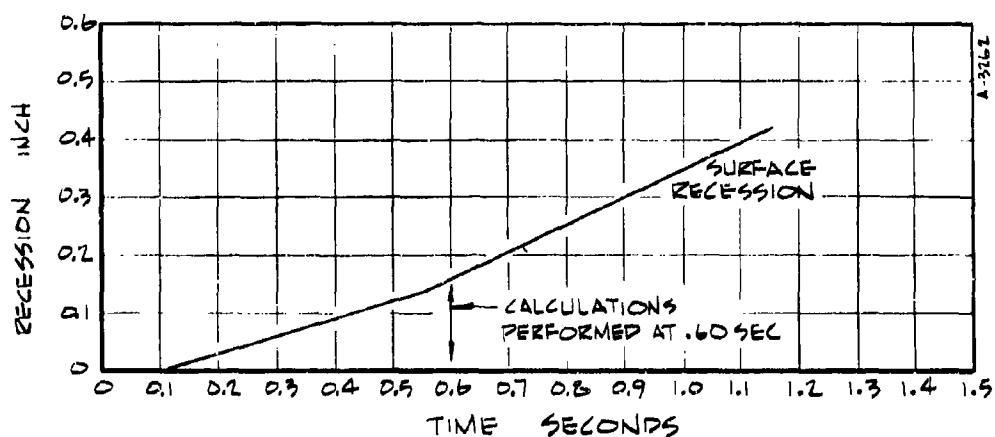
C) POCO GRAPHITE (MODEL 12-2) RENT  
 CONTOUR AT 1.89 SECONDS BLUNT (SEE FIGURE 19C)

FIGURE 20 CONTINUED



D) R-6300 CARBON PHENOLIC (MODEL 103A) RENT  
CONTOUR AT 0.7 SECONDS,  $\theta_c = 43^\circ$ ,  $R_N = .072$  IN

FIGURE 20, CONTINUED



E) R-6300 CARBON PHENOLIC (MODEL 123A) RENT  
CONTOUR AT .06 SECONDS,  $\theta_c = 43^\circ$ ,  $R_N = 0.072$  IN.

FIGURE 20, CONCLUDED

performed may be illustrated by referring to Figure 20a for model G-9 tested in the wave superheater. For this particular case, the contour analyzed was selected to have a  $64^\circ$  cone half angle and a nose radius of 0.06 inch. This contour corresponds approximately to a time of 2.8 sec which is after most shape change has occurred, the surface temperature has leveled out, and the recession rate is relatively constant.

As indicated in Figure 20a, there is considerable uncertainty associated with estimating an effective cone half angle and nose radius from the film data. WSH tested models ablated to somewhat asymmetric shapes as indicated in Figures 19a and b while models tested in the RENT facility (Figures 19c through 19e) displayed only minor asymmetries. The effects on the ablation predictions of uncertainties associated with defining an effective nose contour from the movie film data were assessed by carrying out additional solutions with bracketing values of nose radius and cone half angle. It was found that the effect of these uncertainties on predicted recession rate was from 10 to 15 percent. Detailed results from these solutions are given in Section 3.2.

### 3.2.2 Inviscid Flow Representation

Boundary layer solutions require specification of (1) the model surface pressure distribution, and (2) if shock curvature is great, the shock shape must also be specified in order to properly account for vorticity at the boundary layer edge. A single solution was performed accounting for vorticity and it was concluded that entropy layer effects are negligible for the test conditions and model shapes being considered here (see Table II). Because a detailed shock shape specification was not required it was not necessary to perform numerical inviscid flow field solutions as was required for the ballistic range tests described in Section 3.1.

Pressure distributions for all models were computed employing a corrected form of the pressure distribution correlation suggested in Reference 28. The correlation suggested in Reference 28 gives unsatisfactory results when the free stream pressure (nozzle exit pressure) was significant relative to the model stagnation pressure. The pressure distribution correlation equation employed is given here.

$$\begin{aligned} \bar{P} = \bar{P}_\infty + (1 - \bar{P}_\infty) \cos^2 \theta - (1 - \bar{P}_{FD}) & \left[ \frac{\bar{P}_\infty + (1 - \bar{P}_\infty) \cos^2 \theta - \bar{P}^*}{1 - \bar{P}^*} \right] \\ + \left( 1 - \frac{R_N}{R_{\max}} \right) & \left[ \left( 1 - \frac{S}{S^*} \right) (1 - \bar{P}_\infty) \sin^2 \theta \right. \\ + \frac{1}{2} \frac{S}{S^*} & \left\{ \bar{P}_{FD} - 1 + \frac{S}{S^*} (1 - \bar{P}_\infty) \sin^2 \theta \right. \\ + (1 - \bar{P}_{FD}) & \left. \left[ \frac{\bar{P}_\infty + (1 - \bar{P}_\infty) \cos^2 \theta - \bar{P}^*}{1 - \bar{P}^*} \right] \right\} \left. \right] \end{aligned}$$

where:

$$\bar{P} = \frac{P}{P_{t_2}}$$

$$\bar{P}_{FD} = 1 - (1 - \bar{P}^*) e^{-\lambda} - \frac{1}{16} \left[ \left( \frac{S^*}{S} \right)^2 - e^{-\lambda} \right]$$

$$\lambda = 5 \sqrt{\ln \left( \frac{S}{S^*} \right)}$$

$$\bar{P}^* = \left( \frac{2}{\gamma + 1} \right)^{\frac{\gamma}{\gamma - 1}}$$

$R_{\max}$  is the maximum of either  $R_N$  or  $R^*$

\* denotes sonic condition

$P_{t_2}$  = stagnation point impact pressure

$P_\infty$  = free stream static pressure

The sonic point is located by assuming a Newtonian pressure ratio there which yields:

$$\theta^* = \cos^{-1} \left[ \sqrt{\frac{P^* - P_\infty}{P_0 - P_\infty}} \right]$$

The above pressure distribution equation is used for the stagnation point to the sonic point. A Newtonian  $\bar{P}$  given by

$$\bar{P} = \bar{P}_\infty + (1 - \bar{P}_\infty) \cos^2 \theta$$

is used downstream of the sonic point and up until

$$\left. \frac{dP}{ds} \right|_{\text{Newtonian}} = \left. \frac{dP}{ds} \right|_{\text{Prandtl-Meyer}}$$

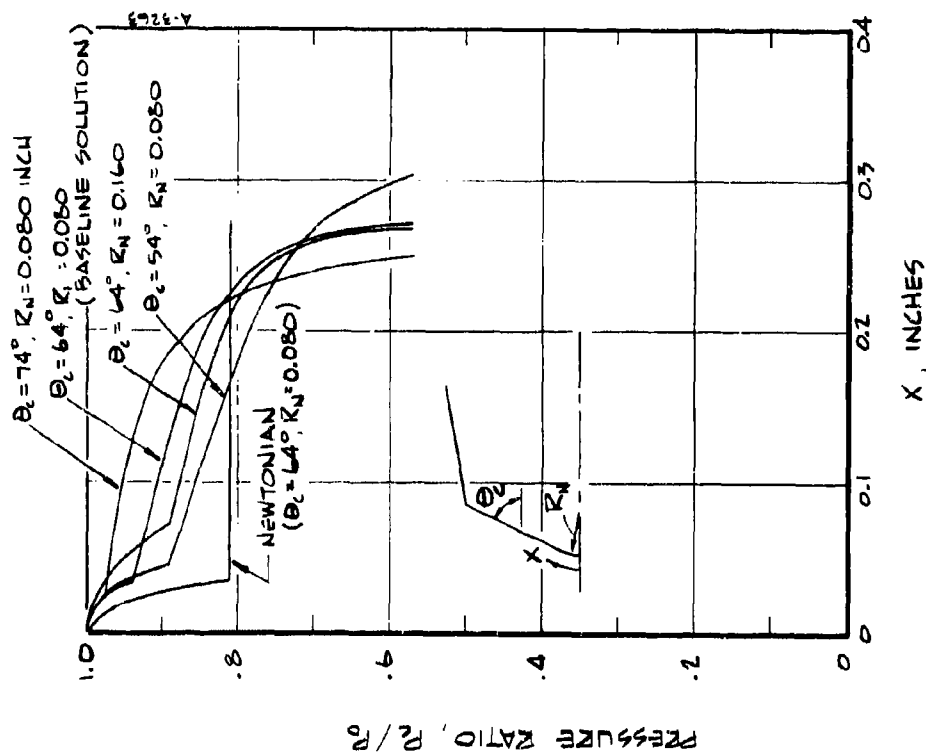
and  $\bar{P}$  is obtained from the Prandtl-Meyer expansion expression downstream of this "match point."

Pressure distributions for all models are shown in Figures 21a through e. In addition to the pressure distribution for the baseline contour for model G-9, Figure 21a shows pressure distributions employed for investigating effects of uncertainties in measurement of cone angle and nose radius as well. Also shown for comparison purposes is the Newtonian pressure distribution for this model. Boundary layer solutions including steady state surface recession rate calculations were performed for all pressure distributions shown in Figures 21a through e.

### 3.2.3 Boundary Layer Solutions

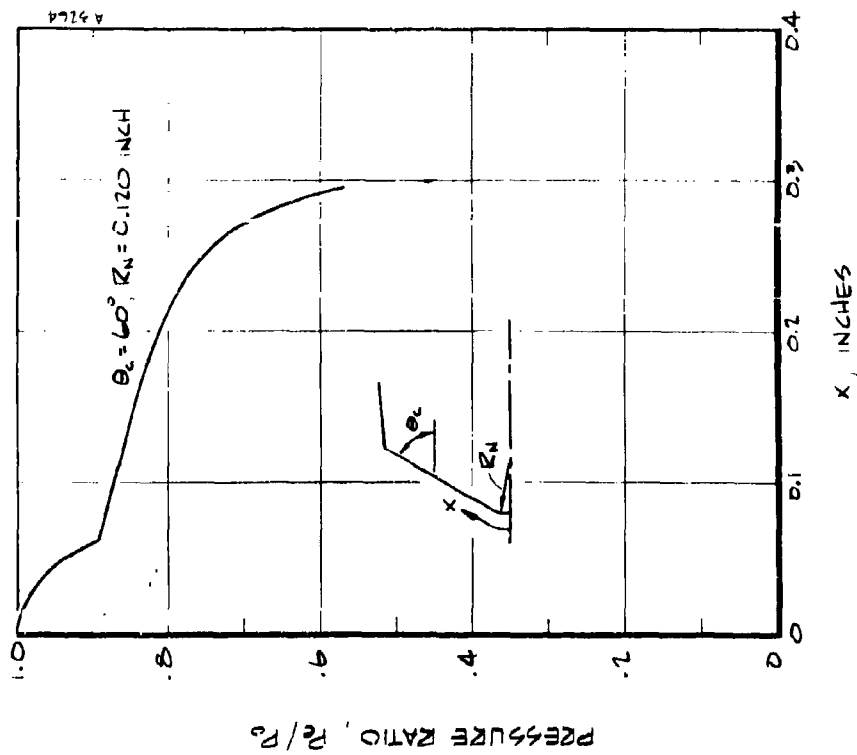
All boundary layer solutions were performed with the BLIMP program. With the exception of one solution performed for model G-9 accounting for entropy layer effects, all solutions were performed assuming the boundary layer edge thermodynamic state was represented by an equilibrium isentropic expansion from stagnation (normal shock) conditions. For all models which assumed a conical nose shape (all but model 12-2 which blunted) boundary layer transition was assumed to occur just past the sphere cone junction. For model 12-2 (POCO graphite tested in the RENT facility) the boundary layer was assumed laminar over the entire nose. A brief study was also conducted to assess the effect of transition location upon predicted recession for the models which assumed a conical shape. Varying the transition location from the stagnation point to just downstream of the sphere cone junction had negligible effect upon predicted recession rate in the mid-cone region.

All solutions but one employed the assumption of equal molecular diffusion coefficients and the neglect of thermal diffusion. One solution was performed with best estimate molecular diffusion coefficients for all species and included thermal diffusion as well. This solution was performed for an R-6300 carbon phenolic model (CP-16) and revealed only a 3 percent effect on predicted



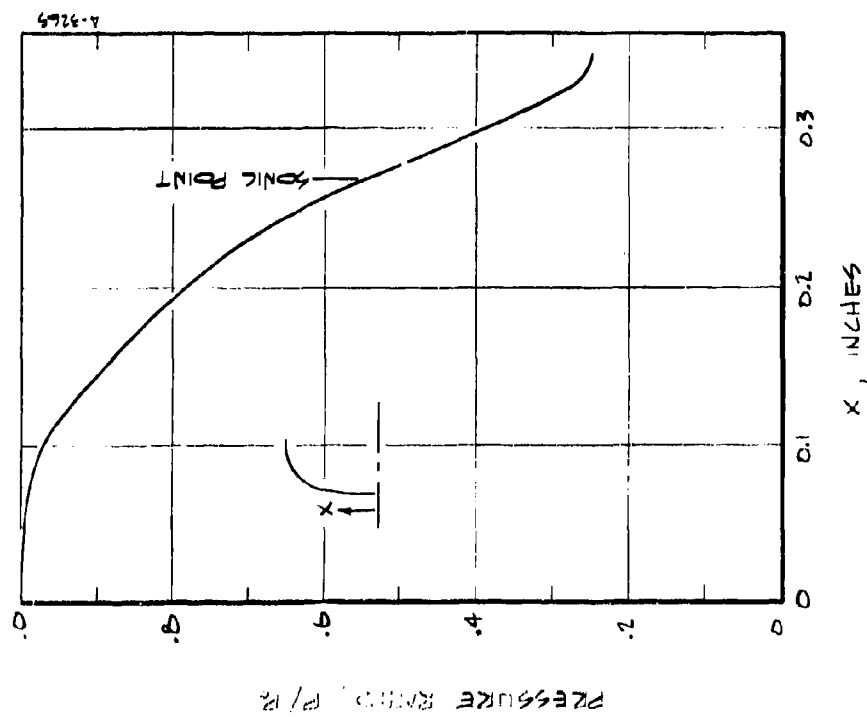
A) POCO GRAPHITE (MODEL 4-9) WAVE SUPERHEATER

FIGURE 21. MODEL PRESSURE DISTRIBUTIONS



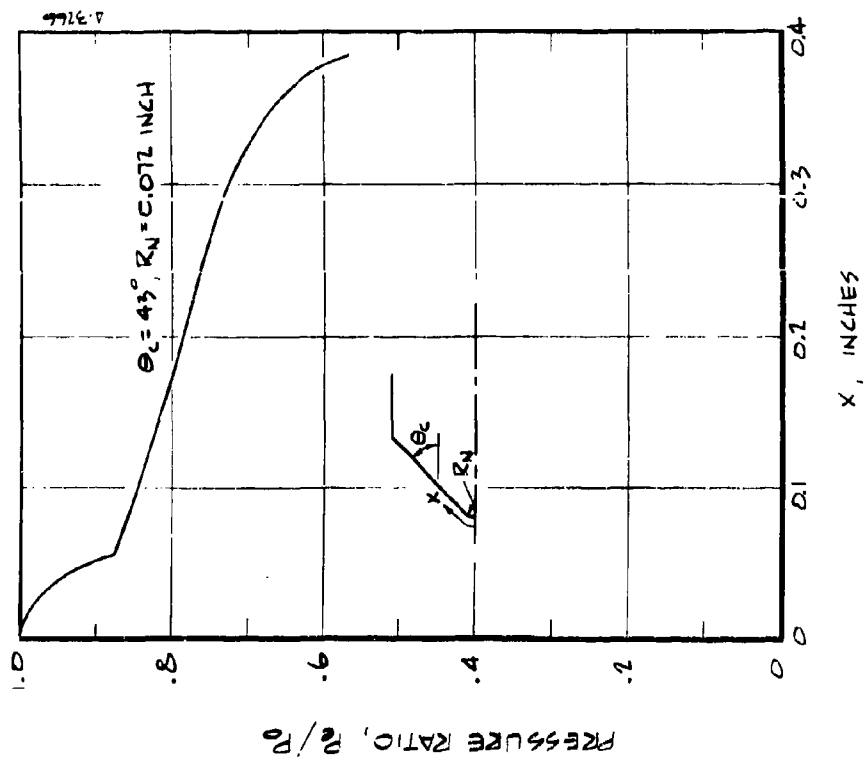
B) R-6300 CARBON PHENOLIC (MODEL CP-16) WAVE SUPERHEATER

FIGURE 21. CONTINUED



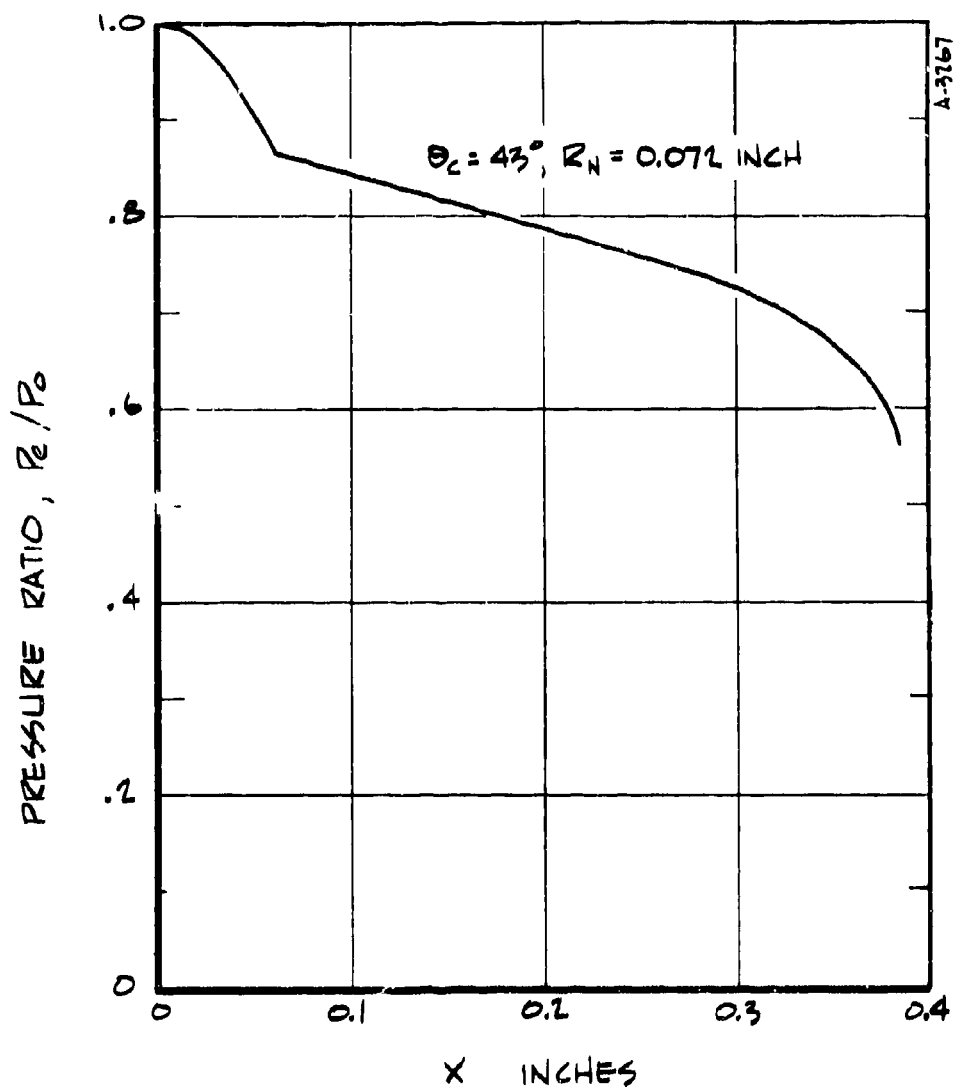
c) POLO GRAPHITE (MODEL 12-2) RENT

FIGURE 21, CONTINUED



d) R-6300 CARBON PHENOLIC (MODEL 103A) RENT

FIGURE 21, CONTINUED



E) R-6300 CARBON PHENOLIC (MODEL 123A) RENT

FIGURE 21, CONCLUDED



recession rate when compared to the equal diffusion calculation for the same model.

Steady state energy and mass balances were assumed for all models. The steady state mass balance implies that the relative quantity of chemical elements being ablated from the surface are in the same ratio as they are in the virgin material. The steady state energy balance assumption implies that the rate of heat conduction into the material from the ablating surface is equal to the product of mass loss rate and enthalpy increase of the ablation material from its initial temperature to the surface temperature.

$$q_w \text{ conduction} = \dot{m}(H_{T_w} - H_{\text{initial}})_{\text{ablation material}}$$

### 3.2.4 Ablation Response

This section presents results directed at assessing the effect of several uncertainties upon predicted ablation response and compares measured to predicted ablation material performance.

#### 3.2.4.1 Effect of Uncertainties

Prior to making predictions for comparing to measured data, an assessment was made of the effect of various uncertainties upon predicted ablation rate. These uncertainties fall into two categories:

##### 1. Experimental Data Uncertainties

- o Inability to precisely measure nose radius from film data
- o Inability to precisely determine the body cone angle from film data
- o Uncertainty in stream total enthalpy in RENT facility

##### 2. Uncertainties in Mathematically Modeling the Physics

- o Location of boundary layer transition
- o Uncertainties in assessing the nose pressure distribution
- o Are entropy layer effects important?
- o Is it necessary to treat unequal molecular diffusion coefficient effects?

With the exception of the total enthalpy uncertainty (2530 Btu/lb bulk enthalpy vs. 5000 Btu/lb on the centerline inferred from heat flux measurements) in the RENT facility, uncertainties investigated generally resulted in less than a 15 percent change in surface recession rate on the conical (turbulent)

portion of the test model. Utilization of the bulk enthalpy rather than the estimated centerline value in the RENT facility resulted in a 35 percent decrease in predicted ablation rate.

The effect of many of the investigated uncertainties upon predicted ablation rate is shown in Figures 22a through e. A tabular summary of the effect of the investigated uncertainties is given in Table III.

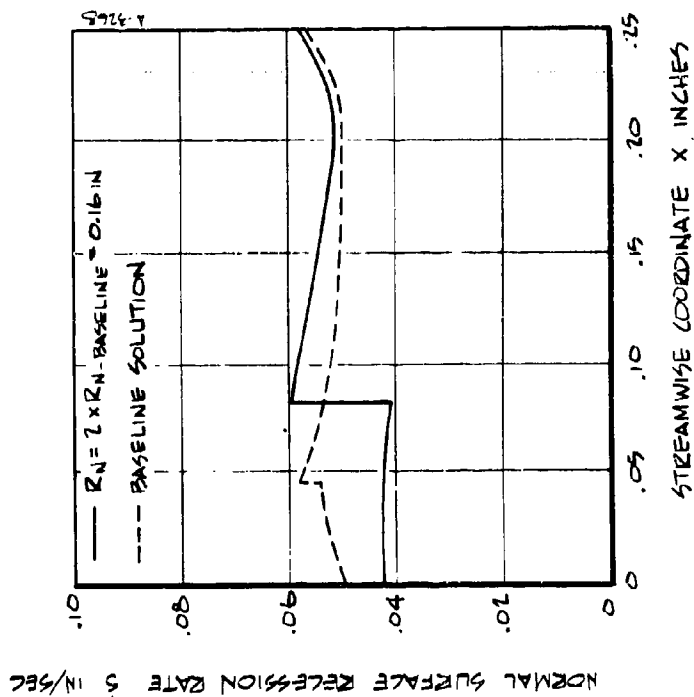
#### 3.2.4.2 Comparison of Predictions with Data

The predicted and measured axial surface recession rates are shown in Figures 23a through e. The axial recession rate is shown in the figures for comparison. The experimental recession rates are all shown as horizontal lines since, at the times analyzed, relatively stable experimental shapes were observed. Predicted and measured stagnation point surface temperatures are also shown for models tested in the wave superheater.

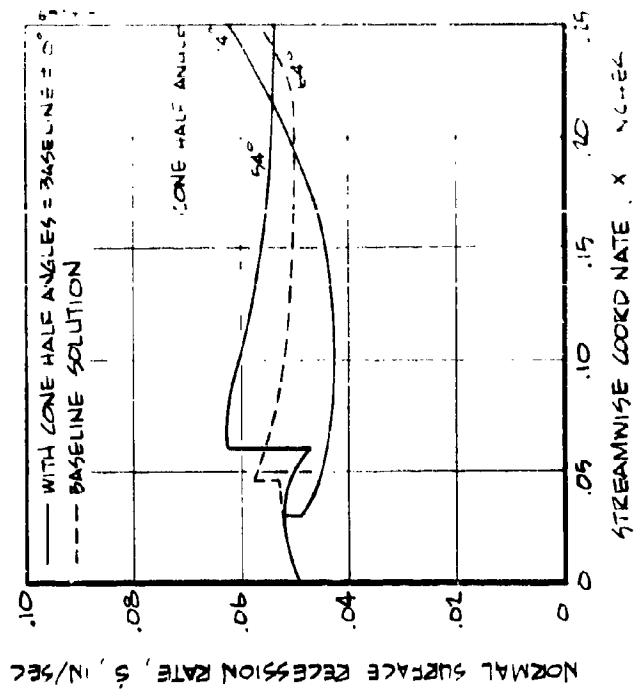
The predicted stagnation point surface temperature for the POCO graphite model in the wave superheater (Model G-9) is about  $350^{\circ}\text{R}$  above the measured value, whereas the corresponding prediction for carbon phenolic is  $1300^{\circ}\text{R}$  above the measurement. It is believed that the large discrepancy in predicted surface temperature for the carbon phenolic model is a result of mechanical erosion.

TABLE III. Summary of calculations performed to assess the influence of various uncertainties on the predicted model ablation responses. The "cone region" refers to the conical surface nearest the stagnation point of a spherically blunted bi-conic, and the "tangent point" refers to the intersection of this cone with the spherical nose.

UNCERTAINTY	CIRCUMSTANCE ANALYZED	MODEL FOR WHICH ANALYSIS WAS PERFORMED	RESULT
nose radius from film data	$R_N = 2 \times \text{nominal } r_N$	G-9	doubling the nose radius decreased the stagnation point recession rate by about 15%, but had a very small effect on the ablation rate over the cone region
nose bi-conic cone angle from film data	angle = nominal angle - $10^\circ$	G-9	ablation rate on forward cone section increased by about 12%
	angle = nominal angle + $10^\circ$	G-9	ablation rate on forward cone section decreased by about 14%
	transition at stagnation point	G-9	yields heating and ablation peak in vicinity of tangent point
transition location for bi-conic nose	transition at tangent point	G-9	yields sharp heating and ablation rate jump at transition
	transition just downstream of tangent point	G-9	yields relative uniform ablation rate for estimated steady state contour
	Newtonian pressure distribution (relative to Dahm-Love correlation, Ref.28, used for other calculations)	G-9	stagnation point recession increased by about 40% with Newtonian, but change in recession in turbulent flow region over cone was much less
pressure distribution representation	entropy layer accounted for in B.L. solution using approximate shock shape	G-9	negligible effect for these conditions
unequal species diffusion coefficients	B.L. solution accounted for unequal species diffusion coefficients and thermal diffusion for carbon-phenolic using the technique of Ref.	CP-16	unequal species diffusion coefficients and thermal diffusion has a small (less than 3%) effect on carbon-phenolic ablation rate for these conditions
enthalpy spike in AFFDL 50MW RENT facility	calculation utilized reported bulk H (2530 BTU/Lbm) while other 50 MW calculations utilized a centerline H of 5000 BTU/Lbm taken from Ref.25	12-2	utilization of bulk H decreased the calculated ablation rate by about 35%



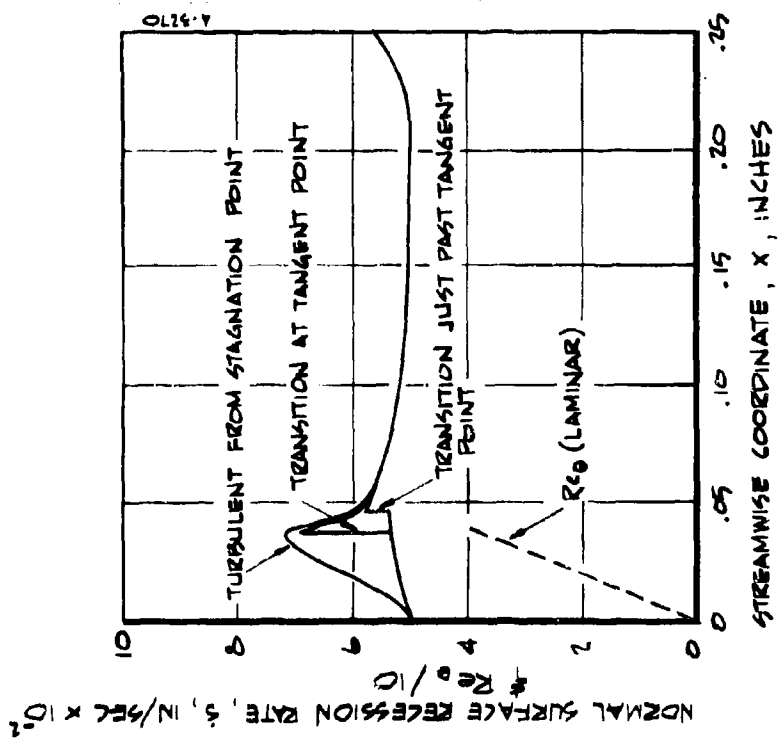
A) NOSE RADIUS  
POCO GRAPHITE (MODEL G-9) WAVE SUPERHEATER



B) CONE HALF ANGLE  
POCO GRAPHITE (MODEL G-9) WAVE SUPERHEATER

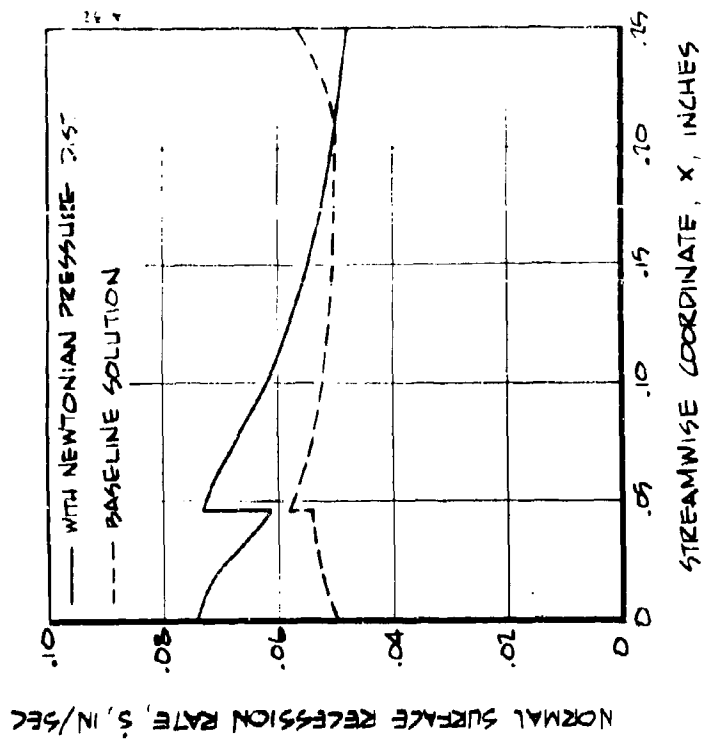
FIGURE 21 EFFECT OF UNCERTAINTIES UPON  
PREDICTED ABLATION RATE

FIGURE 22 CONTINUED



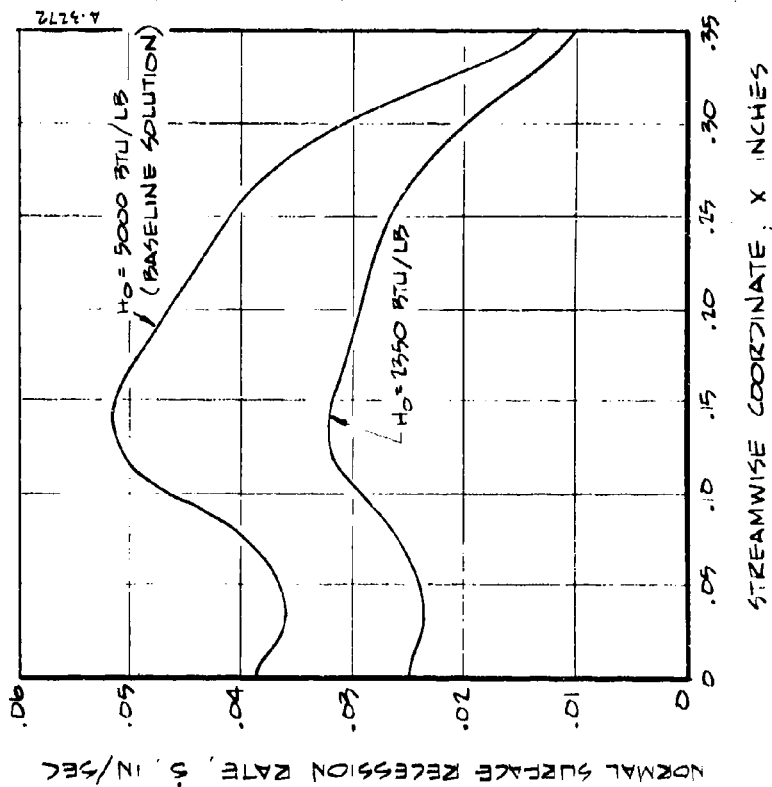
(c) TRANSITION LOCATION  
 POCO GRAPHITE (MODEL G-9) WAVE SUPERHEATER

FIGURE 11, CONTINUED



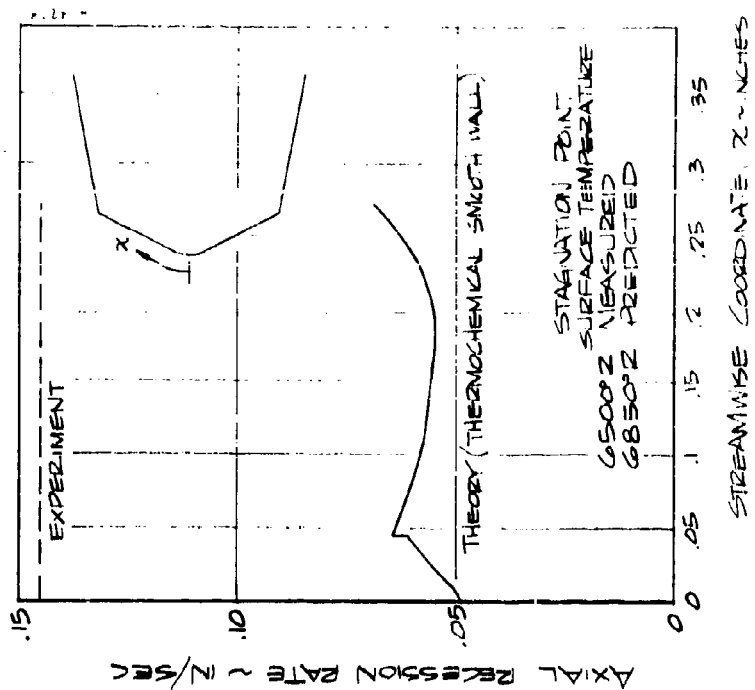
(d) PRESSURE DISTRIBUTION  
 POCO GRAPHITE (MODEL G-9) WAVE SUPERHEATER

FIGURE 12, CONTINUED



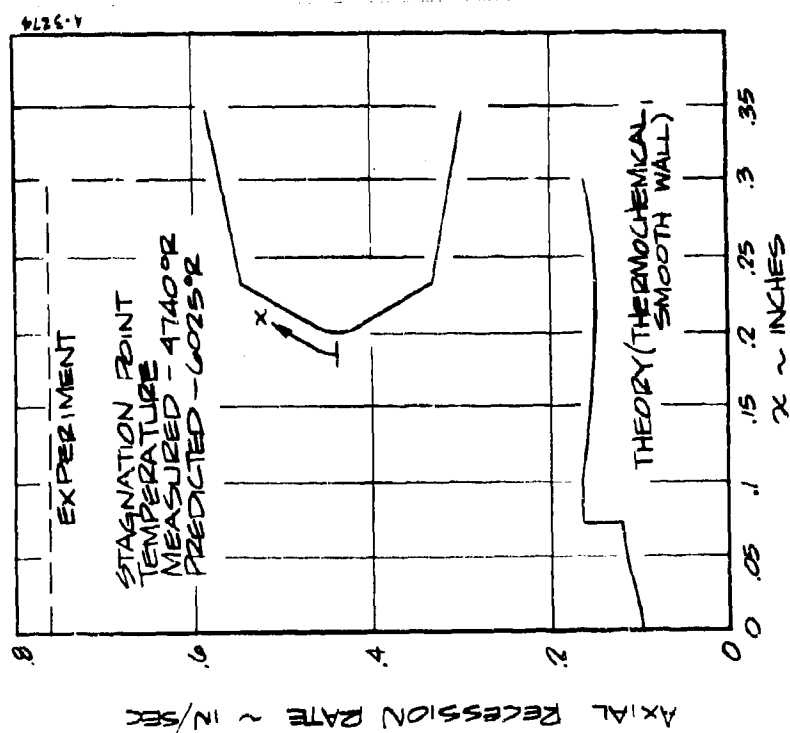
E) STAGNATION ENTHALPY  
POLO GRAPHITE (MODEL 2-2) ZENT

FIGURE 11. CONCLUDED

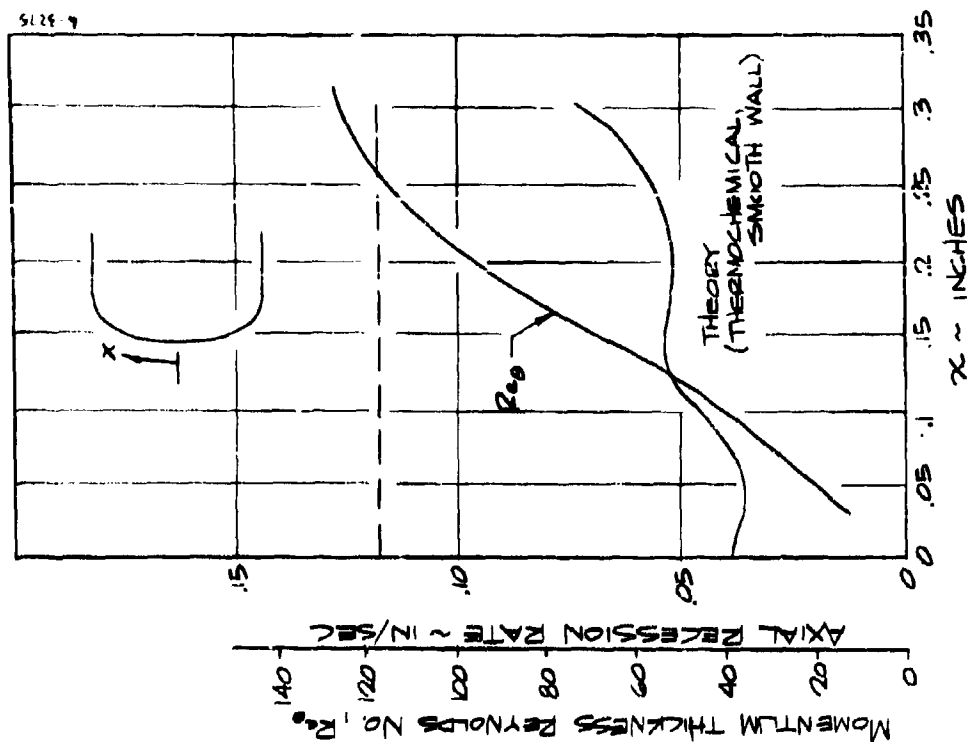


A) POLO GRAPHITE MODEL 3-3  
WAVE SUPER HEATER  
 $P_{e2} = 78$  ATM,  $T_0 = 2103$  BTU/LB

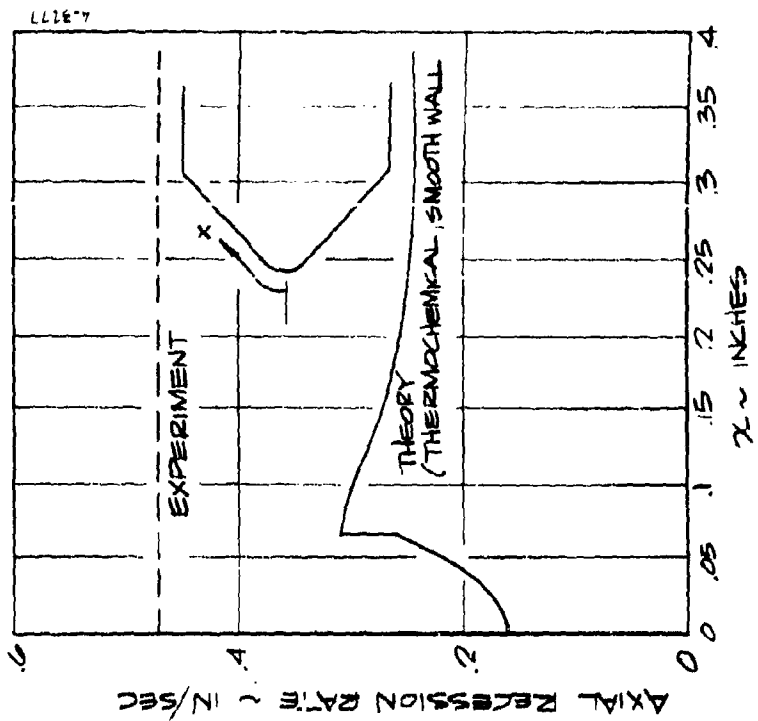
FIGURE 13. COMPARISON OF MEASURED AND  
PREDICTED AXIAL RESSION RATE



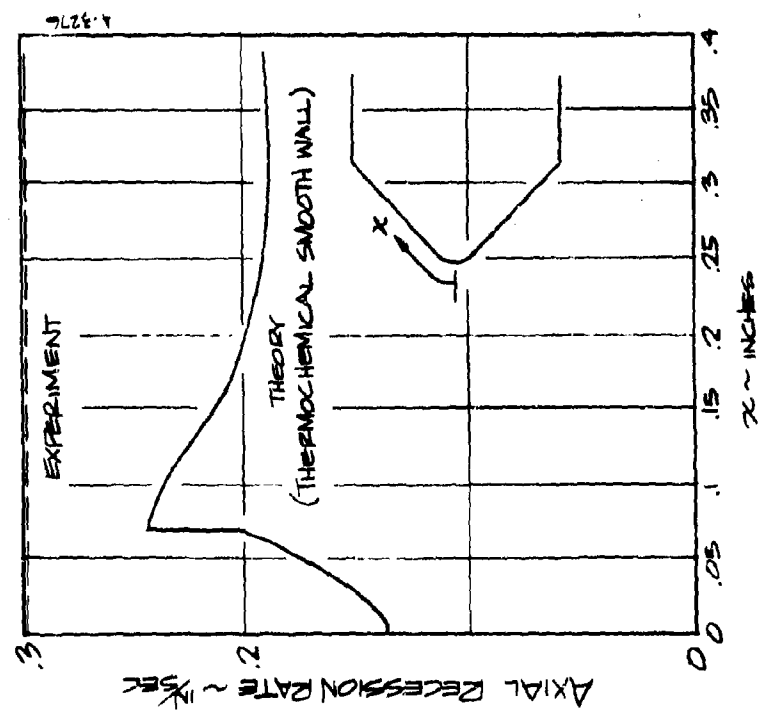
B) R-6300 CARBON PHENOLIC  
MODEL C-16 WAVE SUPERHEATER  
 $Re_2 = 103 \text{ ATM}$ ,  $H_0 = 2164 \text{ BTU/LB}$   
FIGURE 23 (CONTINUED)



C) POCO GRAPHITE MODEL 12-2  
AFFDL 50 INW  
 $Re_2 = 77 \text{ ATM}$ ,  $H_0 = 5000 \text{ BTU/LB}$   
FIGURE 23 (CONTINUED)



E) R-6300 CARBON PHENOLIC  
MODEL 123A, AFFCD 50MW  
 $P_0 = 77 \text{ ATM}$ ,  $H_2 = 5000 \text{ BTU/LBM}$   
FIGURE 23 (CONTINUED)



D) R-6300 CARBON PHENOLIC  
MODEL 103A, AFFCD 50MW  
 $P_0 = 57 \text{ ATM}$ ,  $H_2 = 5000 \text{ BTU/LBM}$   
FIGURE 23 (CONTINUED)



TABLE IV

SUMMARY OF BASELINE STEADY-STATE SMOOTH-WALL  
THERMOCHEMICAL ABLATION RESPONSE PREDICTIONS

MODEL NUMBER	FACILITY	MATERIAL	ABLATION NOSE GEOMETRY (From Film Data)	$H_0$ (Btu/lb)	$P_{t2}$ (atm)	$P_{conc}$ (atm)	$S_{pred.cted}$ Stag.Pt.	$S_{measured}$ X10 <sup>-3</sup>
G-9	WSE	POCO graphite	Bi-Conic; 64° Cone half-angle	2103.	78.	68.	0.345	0.34
CP-16	WSE	R-6300 Carbon Phenolic	Ei-conic; 60° Cone half-angle	2164.	103.	86.	0.132	0.13
12-2	50 MW	POCO graphite	Blunted "larinar" shape	5000.	77.	60**	0.32	0.32**
103A	50 MW	R-6300 Carbon Phenolic	Ei-conic; 43° cone half-angle	5000.	57.	45.	.46	.49
123A	50 MW	R-6300 Carbon Phenolic	Bi-conic; 43° cone half-angle	5000.	77.	60.	.37	.52
1750	Bal.Range.	POCO graphite	Bi-conic; 45° cone half-angle	5150.	100.	54.	.40	.57
1756	Bal.Range.	POCO graphite	Bi-conic; 45° cone half-angle	4450	110	59	.33	.40
1763	Bal.Range.	R-6300 Carbon Phenolic	Bi-conic; 39° cone half-angle	5200	101	41	.41	.51
1861	Bal.Range.	R-6300 Carbon Phenolic	Bi-conic; 37° cone half-angle	6170	77	30	.36	.74

\* Thermal expansion effects not included.

\*\* Nominal average value for the nose.

## SECTION 4

### CONCLUSIONS

The study objective was to perform baseline calculations of ablative model performance considering only thermochemical ablation and representing boundary layer heat-and-mass transport phenomena by smooth-wall relations. The principal conclusion to be reached from this study relates to the discrepancy between these baseline predictions and observed model performance. Some accessory conclusions are also reached which relate to the effect of various uncertainties upon predicted ablation performance.

Table IV summarizes results of the study in the form of predicted-to-measured recession rate ratio for the model stagnation points and mid-cone sections. This ratio is plotted as a function of local surface pressure in Figure 24. With the exception of three ballistic range stagnation point predictions all data correlate well with local pressure. It is noted that inclusion of thermal expansion effects would tend to bring these points in line with the correlation; however, some of the other ballistic range predictions would not correlate as well if thermal expansion effects were included. They are not included in the correlation because significant uncertainty exists in the magnitude of thermal expansion as a result of ill-defined high temperature property data.

It is concluded that surface roughness effects and mechanical ablation effects become increasingly important as pressure increases. The choice of pressure as the correlation parameter here is primarily in the interest of expedience. A detailed effort to correlate the data in terms of more fundamental parameters was not within the study scope. Other parameters which should be considered include surface temperature, rough wall shear and perhaps pressure gradient.

The effects of various experimental uncertainties upon predicted smooth wall thermochemical ablation are summarized in Table III. It is concluded that uncertainties in transition location and nose radius have a negligible effect upon predicted turbulent cone ablation rate. Similarly the effects of unequal species diffusion coefficients and shock layer vorticity have negligible effects for models tested in the wave superheater and RENT facilities. A 10 to

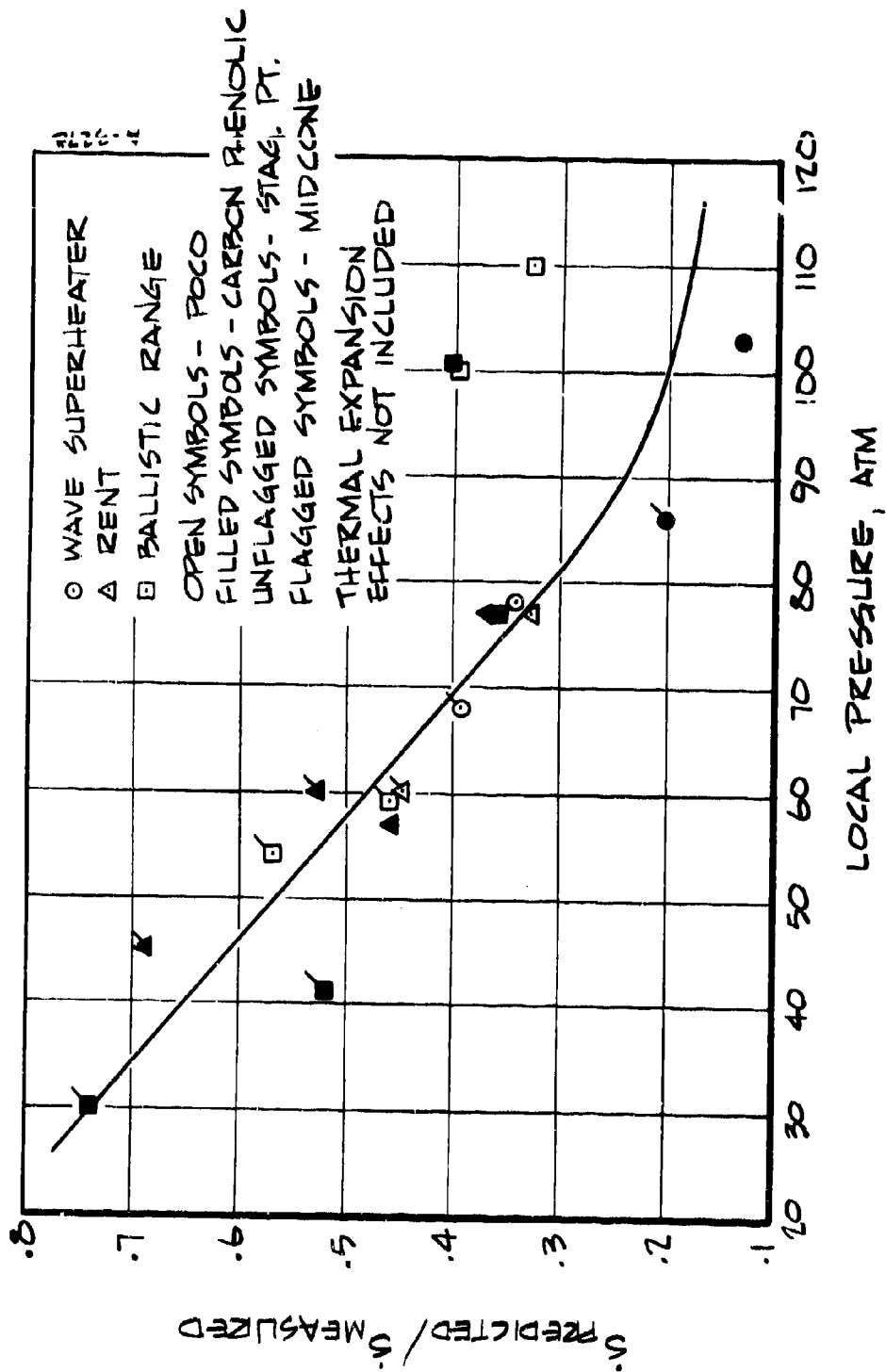


FIGURE 14. CORRELATION OF PREDICTED TO MEASURED RECESSION RATE WITH LOCAL PRESSURE

15 percent error in predicted cone ablation rate is associated with nominal uncertainties in cone half angle and with utilization of an approximate (Newtonian) pressure distribution. Vorticity effects are very important over the entire conic surface for models tested in the ballistic range. Because fundamental data is lacking upon which to base a turbulent prediction with strong edge velocity gradients (normal to the boundary layer edge) these predictions should be viewed to have a 10 to 30 percent uncertainty.

# REFERENCES

1. Fisher, L.E.: High Quality Ablation Program, SAMSO-TR-62-299, November 1969
2. Grabowsky, W.R., and Strickler, R.L.: High Quality Ablation Experimental Results -- Phase I. Aerospace TR-0066(S5816-74)-2, SAMSO-TR-215, April 1970.
3. Personal Communication, Sam Breshears, Aerospace Corporation, San Bernardino, California, August 1970.
4. Personal Communication, Sam Breshears, Aerospace Corporation San Bernardino, California, January 1970.
5. Personal Communication, R. M. Raper, AEDC (ARO, Inc.), Tullahoma, Tennessee, April 1970.
6. Kendall, R.M.: A General Approach to the Thermochemical Solution of Mixed Equilibrium-Nonequilibrium, Homogeneous or Heterogeneous Systems, Aerotherm Corporation, Mt. View, Calif., Report No. 66-7, Part V, 14 March 1967 (also NASA CR 1064).
7. Kendall, R.M., Rindal, R.A., and Bartlett, E. P.: A Multicomponent Boundary Layer Chemically Coupled to an Ablating Surface, AIAA Journal, Vol. 5, No. 6, June 1967, pp. 1063-1071.
8. Powars, C.A. and Kendall, R.M.: User's Manual, Aerotherm Chemical Equilibrium Code, Aerotherm Corporation, Mt. View, Calif., May 1969.
9. Moretti, G. and Abbett, M.: A Time-Dependent Computational Method for Blunt Body Flows, AIAA Journal, Vol. 4, No. 12, pp. 2136-2141.
10. Abbett, M.J.: Inviscid Equilibrium Air Flow about Blunted Cones at Incidence - Analysis and User's Manual, Aerotherm Corporation, Mt. View, Calif., Report No. UM-70-20, 30 June 1970.
11. Johnson, James: Investigation of the Low Speed Fixed Geometry Scramjet, Part I - Inlet Design Practice Manual, General Applied Science Labs, Westbury, N.Y., Report No. AFAPL-TR-68-7, February 1968.
12. Kendall, R.M. and Bartlett, E.P.: Nonsimilar Solution of the Multicomponent Laminar Boundary Layer by an Integral Matrix Method, AIAA Journal, Vol. 6, No. 6, June 1968, pp. 1089-1097.
13. Kendall, R.M. and Bartlett, E.P.: An Analysis of the Coupled Chemically Reacting Boundary Layer and Charring Ablator, Aerotherm Corporation, Mt. View, Calif., Report No. 66-7, Part I, 14 March 1967 (also NASA CR 1060).
14. Bartlett, E.P. and Kendall, R.M.: Nonsimilar Solution of the Multicomponent Laminar Boundary Layer by an Integral Matrix Method, Aerotherm Corporation, Mt. View, Calif., Report No. 66-7, Part III, 14 March 1967 (also NASA CR 1062).

15. Anderson, Larry W. and Kendall, Robert M.: A Nonsimilar Solution for Multi-component Reacting Laminar and Turbulent Boundary Layer Flows Including Transverse Curvature, Aerotherm Corporation, Mt. View, Calif., Report No. 69-54, 30 October 1969.
16. Bartlett, Eugene P. and DeBlaye, Christian: User's Manual, Boundary Layer Integral Matrix Procedure (BJIMP), Aerotherm Corporation, Mt. View, Calif., Report No. 68-42, 15 October 1968.
17. Bartlett, E.P. and Anderson, L.W.: An Evaluation of Ablation Mechanisms for the Apollo Heat Shield Material, Aerotherm Corporation, Mt. View, Calif., Report No. 68-38, Part II, 15 October 1968.
18. Moyer, C.B. and Rindal, R.A.: Finite Difference Solution for the In-Depth Response of Charring Materials Considering Surface Chemical and Energy Balances, Aerotherm Corporation, Mt. View, Calif., Report No. 66-7, Part II, 14 March 1967, (also NASA CR 1061, June 1968).
19. User's Manual, Aerotherm Charring Material Thermal Response and Ablation Program, Version 3, Vol. I - Program Description and Sample Problems, Aerotherm Corp., Mt. View, Calif., Report No. UM-70-14, April 1970.
20. Baker, D.L., Wool, M.R., and Schaefer, J.W.: A Dynamic Technique for Determining the Thermal Conductivity of Charring Materials, Eighth Conference on Thermal Conductivity, October 7-11, 1968, Thermophysical Properties Research Center, West Lafayette, Ind.
21. Moyer, C.B.: Axi-symmetric Transient Heating and Material Ablation Program (ASTHMA), Description and User's Manual, Aerotherm Corporation, Mt. View, Calif., Report No. 68-27, 15 January 1968.
22. Weiler, F.C.: Anisotropic Plasticity via the Finite Element Method, Aerotherm Corp., Technical Report -- to be published.
23. Weiler, F.C. and Rodriguez, D.A.: A Study of Advanced Methods of Anisotropic, Elastic-Plastic-Thermal Stress Analysis for Bodies of Revolution, Aerotherm Report No. 70-7, March 1970 (see also AFML Technical Report No. 70-133).
24. Reentry Materials Handbook, Aerospace Corp., San Bernardino, Calif.
25. Green, K.A., Kennedy, W.S., Rindal, R.A., and Powars, C.A.: Second Quarterly Progress Report, AFFDL 50 MW RENT Facility Calibration -- for the period Feb. 12 - June 12, 1970, Aerotherm Corp., Mt. View, Calif.
26. Kennedy, W.S., Powars, C.A., Rindal, R.A. and Green, K.A.: First Quarterly Report, AFFDL 50 MW RENT Facility Calibration - for the period Oct. 12, 1969 through Feb. 12, 1970, Aerotherm Corp., Mt. View, Calif.
27. Powars, C.A. and Rindal, P.A.: A Study of the Effects of Test Stream Nonuniformities on Ablative Model Response. Aerotherm TN-70-17, June 1970.
28. Moyer, C.B., Anderson, L.W. and Dahm, T.J.: A Coupled Computer Code for the Transient Thermal Response and Ablation of Non-Charring Heat Shields and Nose Tips. Aerotherm Final Report 69-60, August 1969.